

Silica-rich lavas in the oceanic crust: experimental evidence for fractional crystallization under low water activity

Martin Erdmann^{1,2}  · Jürgen Koepke¹

Received: 20 May 2016 / Accepted: 30 August 2016 / Published online: 15 September 2016
© Springer-Verlag Berlin Heidelberg 2016

Abstract We experimentally investigated phase relations and phase compositions as well as the influence of water activity ($a_{\text{H}_2\text{O}}$) and redox conditions on the equilibrium crystallization path within an oceanic dacitic potassium-depleted system at shallow pressure (200 MPa). Moreover, we measured the partitioning of trace elements between melt and plagioclase via secondary ion mass spectrometry for a highly evolved experiment ($\text{SiO}_2 = 74.6 \text{ wt}\%$). As starting material, we used a dacitic glass dredged at the Pacific-Antarctic Rise. Phase assemblages in natural high-silica systems reported from different locations of fast-spreading oceanic crust could be experimentally reproduced only in a relatively small range of temperature and melt-water content ($T \sim 950 \text{ }^\circ\text{C}$; melt $\text{H}_2\text{O} < 1.5 \text{ wt}\%$) at redox conditions slightly below the quartz–fayalite–magnetite buffer. The relatively low water content is remarkable, because distinct hydrothermal influence is generally regarded as key for producing silica-rich rocks in an oceanic environment. However, our conclusion is also supported by mineral and melt chemistry of natural evolved rocks; these rocks are only congruent to the composition of those experimental phases that are produced under low $a_{\text{H}_2\text{O}}$. Low FeO contents under water-saturated conditions and the characteristic enrichment of Al_2O_3 in high $a_{\text{H}_2\text{O}}$ experiments, in particular, contradict natural observations,

while experiments with low $a_{\text{H}_2\text{O}}$ match the natural trend. Moreover, the observation that highly evolved experimental melts remain H_2O -poor while they are relatively enriched in chlorine implies a decoupling between these two volatiles during crustal contamination.

Keywords Crystallization experiments · Phase equilibria · Differentiation · Dacite · Fast-spreading mid-ocean ridge · Oceanic plagiogranite

Introduction

Although the extrusive crust, which formed at oceanic spreading centers with intermediate- to fast-spreading ridges, is regarded as basaltic, at some places silicic rocks such as andesites, dacites and rhyodacites have erupted (e.g., Byerly et al. 1976; Fornari et al. 1983; Perfit and Fornari 1983; Hekinian et al. 1999; Haase et al. 2005; Stakes et al. 2006; Wanless et al. 2010, 2011; Freund et al. 2013). The total amount of these evolved rocks is small, but they are widely distributed within the upper oceanic crust. In addition to evolved extrusive rocks, high-silica rocks also occur in the lower oceanic crust, mostly as small intrusions and veins, known from ophiolites (see compilation in Koepke et al. 2004) but also sampled in the recent oceanic crust (e.g., Dick et al. 2000; Wilson et al. 2006; Silant'yev et al. 2014; Erdmann et al. 2015).

The generation of highly evolved, silicic magmas within the oceanic crust has been attributed to various magmatic processes and is, in many cases, related to a complex mix of different formation processes. The question of whether partial melting (Koepke et al. 2007; Brophy 2009; France et al. 2010, 2014; Erdmann et al. 2015), extensive fractional crystallization (Toplis and Carroll 1996; Berndt et al.

Communicated by Jochen Hoefs.

✉ Martin Erdmann
m.erdmann@mineralogie.uni-hannover.de

¹ Institut für Mineralogie, Leibniz Universität Hannover, Callinstr. 3, 30167 Hannover, Germany

² CRPG, UMR 7358, CNRS, Université de Lorraine, 15 rue Notre Dame des Pauvres, 54501 Vandœuvre-lès-Nancy, France

2005; Brophy 2008) and/or accompanying assimilation of crustal material (Haase et al. 2005; Wanless et al. 2010, 2011; Freund et al. 2013) is the main process in felsic melt generation is discussed at length in the literature. Magma mixing (Sinton and Detrick 1992) and liquid immiscibility (Veksler et al. 2007; Charlier et al. 2013) are additional potential generation processes.

For the experimental simulation of felsic melt generation in the oceanic crust, it is useful to concentrate on one of the described magmatic processes. In previous experimental studies, end-member processes for felsic melt generation within oceanic spreading centers under shallow pressures (<200 MPa) were investigated by using basaltic or gabbroic starting material, for example by simulating partial melting (Beard and Lofgren 1991; Koepke et al. 2004; France et al. 2010, 2014; Erdmann et al. 2015), crystallization processes (Juster et al. 1989; Berndt et al. 2005; Feig et al. 2006, 2010) and liquid immiscibility (Dixon-Spulber and Rutherford 1983; Charlier et al. 2013). Other studies focused on calc-alkaline differentiation trends (Sisson and Grove 1993) or phase relations in dry or hydrous ferrobasalt (Toplis and Carroll 1995; Botcharnikov et al. 2008) via crystallization experiments.

Here, we simulate the process of equilibrium crystallization in a low potassium, oceanic dacitic system by investigating phase relations and phase compositions derived from crystallization experiments. Moreover, we investigate the influence of water activity ($a_{\text{H}_2\text{O}}$) and redox conditions on the crystallization path within this system. As starting material, we used a dacitic glass dredged at the Pacific-Antarctic Rise (PAR). The evolved lavas from the PAR, including the starting material of this study, are considered to be products of assimilation–fractional crystallization processes (Haase et al. 2005; Freund et al. 2013). With this experimental work, we fill a gap in phase relation studies on evolved rocks from the oceanic crust, which are characterized by formation under shallow pressure in a relatively dry, potassium-depleted system. Another purpose of this paper is to present coefficients for trace element distribution between crystals and a dacitic melt for modeling magmatic formation and evolutionary processes in such a special, shallow mid-oceanic ridge environment. Up to now, experimental phase relations studies in oceanic high-SiO₂ lavas have only existed for significantly higher pressure and more potassium-enriched systems (see references below).

Methods

Starting material from the PAR

Submarine samples were dredged along the fast-spreading PAR between 36°S and 40.5°S in 2001, during the SO157

expedition with the German research vessel RV SONNE. These samples show a wide spectrum of lithologies, from basaltic to andesitic–dacitic composition (Haase et al. 2005). The PAR is intersected by the Foundation Seamount Chain at 37°S which probably formed above a mantle plume.

As starting material we used the sample SO157-3DS1 representing a dacitic, sparsely phyrlic glass, which can be regarded as an evolved end member in the magmatic evolution of the PAR from mid-ocean ridge basalt (MORB) to felsic melts (analysis of the remelted glass is presented in Table 1). The mineral assemblage in this sample consisted of small (~0.2 mm) plagioclase and clinopyroxene phenocrysts in a glassy matrix with accessory opaques. Detailed petrographical and geochemical information for sample 3DS1 and other characteristic evolved lavas from the PAR are presented by Haase et al. (2005) and Freund et al. (2013).

Experimental methods

The experimental procedure is described in detail by Erdmann and Koepke (2016) who used the same starting material. Here, we give a brief summary of the applied procedure. The crushed and ground sample was fused twice at 1600 °C, and the homogeneity of the resulting glass was checked by electron microprobe. To ensure a minimal pore volume, the Au capsules were filled with 40 mg of glass powder consisting of two different fractions (<125 and 125–200 μm) and a defined amount of fluid. In order to study the influence of water, $a_{\text{H}_2\text{O}}$ of the experiments was fixed via a mixture of (distilled) water and CO₂ (by using silver oxalate, Ag₂C₂O₄). Five experiments can be performed simultaneously during one run (at defined P , T , f_{H_2}). Four experiments were fluid-saturated with different H₂O–CO₂ compositions: pure H₂O ($X_{\text{H}_2\text{O}} = 1$, water-saturated), $X_{\text{H}_2\text{O}} = 0.6$, $X_{\text{H}_2\text{O}} = 0.2$ and pure CO₂ ($X_{\text{H}_2\text{O}} = 0$). An additional experiment was performed in which the influence of seawater was simulated by adding a fluid composed of distilled water with 3.2 wt% NaCl (also fluid-saturated; all experiments with 5 % total fluid).

All experiments in the high-temperature range (i.e., 1030–910 °C) were performed in two different vertically mounted internally heated pressure vessels (IHPVs) at the high-pressure laboratory in Hannover; both IHPVs are equipped with a rapid quench system to prevent the formation of meta-stable quench phases (Berndt et al. 2002). One of these apparatuses is additionally equipped with a Shaw membrane for controlling f_{O_2} via the defined addition of H₂ (for details see Berndt et al. 2002).

The chosen pressure (pure Ar as pressure medium) for the experiments was 200 MPa, which is a typical value for magma storage conditions at the base of fast-spreading

Table 1 Starting compositions in wt%

Sample	SiO ₂	TiO ₂	Al ₂ O ₃	FeO	MnO	MgO	CaO	Na ₂ O	K ₂ O	P ₂ O ₅	Cr ₂ O ₃	SO ₂	Cl	Total
Freund et al. (2013)														
PAR-SO157-3DS1	61.95	1.02	13.54	7.97	0.12	1.57	4.47	4.49	1.27	0.29	0.03	0.06	0.96	97.74
Freund et al. (2013), normalized to 100 wt%														
PAR-SO157-3DS1	63.38	1.04	13.85	8.15	0.12	1.61	4.57	4.59	1.30	0.30	0.03	0.06	0.99	100.00
remelted sample PAR-SO157-3DS1 for this study, normalized to 100 wt%														
PAR-ME	65.00	0.95	14.20	7.87	b.d.	1.46	4.58	4.45	1.18	b.d.	n.a.	b.d.	0.32	100.00
Cadoux et al. (2014), normalized to 100 wt%														
Santorini—Cape Riva	67.58	0.68	15.43	4.35	0.13	1.09	3.00	4.90	2.61	0.23				100.00
Holtz et al. (2005), normalized to 100 wt%														
Unzen	64.58	0.70	15.84	5.04	0.09	2.65	4.86	3.60	2.50	0.14				100.00
Costa et al. (2004), normalized to 100 wt%														
San Pedro	66.33	0.52	16.25	3.90	0.10	1.71	4.05	4.21	2.76	0.16				100.00
Scaillet and Evans (1999), normalized to 100 wt%														
Pinatubo	65.03	0.53	16.42	4.35	2.38	0.10	5.20	4.47	1.53					100.00

b.d. below detection limit of the electron microprobe, *n.a.* not analyzed

oceanic crust. Additionally, near-liquidus experiments were also performed at lower pressure (i.e., 100 and 50 MPa) in order to simulate magma ascent and to study the influence on pressure-sensitive phases. In order to consider the influence of fO_2 on phase relations and compositions, especially on the stability of FeTi oxides, two experimental series were performed. For this, different proportions of H₂ were added to the pressure medium (Ar) corresponding to an fO_2 of QFM+1 (QFM = log fO_2 buffered by the quartz–fayalite–magnetite assemblage; hereafter labeled as “reducing” conditions) and QFM+3.2 (“intrinsic” conditions of the vessel; hereafter labeled as “oxidizing” conditions) for the water-saturated condition. Since in water-undersaturated experiments fH_2O and, thus, fO_2 decrease with aH_2O , and most of our experiments were water-undersaturated, the prevailing fO_2 in our experiments was generally more reduced. To calculate fO_2 under water-undersaturated conditions, we followed Berndt et al. (2005; see below). Considering the variation of aH_2O in our runs, the estimated values of fO_2 in our experiments varied between ~QFM–3.4 and ~QFM+3.2. Temperatures varied between 1030 °C (hyper-liquidus for high-water-content/reducing conditions; near-liquidus for lower-water-content/reducing conditions and for high-water-content/oxidizing conditions) and 910 °C (near-solidus/solidus) in steps of 40 °C.

Near-solidus experiments (i.e., $T \leq 850$ °C) were performed in cold sealed pressure vessels (CSPVs) at 200 MPa (H₂O as pressure medium). In these vessels, redox conditions are buffered by the steel-containing nickel autoclave material. The fO_2 in the experiments corresponds to NNO (NNO = log fO_2 buffered by the nickel–nickel oxide transition) which is identical to Δ QFM+0.7. Therefore, these experiments are in the same range as experiments performed under reducing conditions in the IHPV and, thus, directly comparable to each other.

For two experimental series at 950 °C/high initial fO_2 and 800 °C/low initial fO_2 , the temperature cycling technique was applied in order to generate larger crystals and melt pools (for details see Erdmann and Koepke 2016). Hence, for these conditions a larger data set is available and in situ trace element analyses were enabled due to larger phases (see below).

The aH_2O was calculated following the thermodynamic model of Burnham (1979, 1994). It should be noted that the model of Burnham (1979) slightly overestimates aH_2O (e.g., Botcharnikov et al. 2005). Our experiments were performed with known fH_2 but variable fH_2O . Therefore, fO_2 is not strictly constant from one capsule to the other. Decreasing fH_2O along with decreasing XH_2O causes a lowering of fO_2 (Scaillet et al. 1995; Botcharnikov et al. 2005). Knowing fH_2O (calculated from thermodynamically defined conditions at certain temperature) and fH_2 (pH_2 monitored during experiments), fO_2 can be computed. Here fH_2 is

calculated using the set ΔQFM value for water-saturated conditions of the IHPV. With given pressure, temperature and intrinsic pH_2 conditions measured by the Shaw membrane technique, we calculated ΔQFM for water-saturated conditions using the models of Pitzer and Sterner (1995), Shaw and Wones (1964) and Schwab and Küstner (1981). All experimental conditions are summarized in the experimental protocol in Table 2.

Analytical methods

These analytical methods are the same as described by Erdmann and Koepke (2016) who used a small subset of experiments presented here for a methodological study. The run products (glass and minerals) were analyzed with the Cameca SX 100 electron microprobe at Leibniz Universität Hannover. To analyze the crystals, the following operating conditions were chosen: 15 kV high voltage, 15 nA beam current, 10 s counting time on peak and 10 s on background, focused beam. For the analysis of the remaining water-bearing glass, which is problematic due to “alkali-loss” effects, a special procedure was applied following Koepke et al. (2004). The beam current was set to 4 nA; the counting time varied for different elements and was 4 s for K, 8 s for Si, Al, Ti and Fe, 10 s for Na and Zr, 12 s for Mg, 16 s for Ca and 30 s for Ba, P, S, Cl and Mn. Background counting time was always same as the peak time. Whenever possible, a defocused beam with a spot size of 5, 10 or 20 μm was used, and Na loss was checked by comparing the results of measurements with different beam sizes on identical glasses of an experimental sample with larger melt pools. Standard glasses with compositions similar to the experimental glasses and with known water contents have been used for estimating the water contents in the experimental glasses by the “by-difference” method (Devine et al. 1995). When melt pools were large enough, melt-water contents were double checked by Karl Fischer titration (KFT; for crystal-free samples) and Fourier transform infrared spectroscopy (FTIR; all samples with melt pools larger $30 \times 30 \mu\text{m}$).

For one experiment (#110), trace elements of melt and plagioclase were analyzed with a Cameca IMS-1270 secondary ion mass spectrometer (SIMS) at the Centre de Recherches Pétrographiques et Géochimiques in Nancy, France. An O^- primary beam with an intensity of 5–30 nA was used at an acceleration voltage of 13 kV. The secondary beam was accelerated with 10 kV, and we analyzed with a mass resolving power of 8000. The energy offset was set to 0 V with a 40 eV energy window. The beam size was between 20 and 30 μm with a slightly oval shape. A reflected light microscope was used to seek the point of interest on the sample and points were checked after measurement using backscattered electron (BSE) images with

an electron probe microanalysis (EPMA). One analysis consists of six cycles, each starting from mass ^{28}Si and increasing to ^{30}Si , ^{47}Ti , ^{85}Rb , ^{88}Sr , ^{89}Y , ^{90}Zr , ^{93}Nb , ^{138}Ba , ^{139}La , ^{140}Ce , ^{142}Ce , ^{146}Nd , ^{147}Sm , ^{151}Eu , ^{152}Sm , ^{153}Eu and finally ^{181}Ta with mass 27.7 and 29.5 as background. For data processing, ^{30}Si was used as reference mass, and the Basalt, Hawaiian Volcano Observatory (BHVO)-2-G standard (Wilson 1997; Ila and Frey 2000; Gao et al. 2002; Raczek et al. 2003; Strnad et al. 2005) was used for calibration. To provide high-quality data, standard measurements were taken between every analytical session. Data were corrected for oxide interferences following the principle of Fahey et al. (1987) and Hellebrand et al. (2002).

Experimental results

Phase relations

Phase relations were studied using IHPVs in the high-temperature range from 1030 to 910 $^\circ\text{C}$ under both oxidizing conditions (i.e., $\Delta\text{QFM}+3.2$ at $a\text{H}_2\text{O} = 1$) and reducing conditions (i.e., $\Delta\text{QFM}+1$ at $a\text{H}_2\text{O} = 1$). The latter case corresponds more closely to the natural system, in an environment where fractionated, MORB-derived melts interact with a hydrothermally altered oceanic crust. For the 850–750 $^\circ\text{C}$ temperature range, only one set of experiments was performed using the CSPVs under $f\text{O}_2$ corresponding to $\sim\Delta\text{QFM}+1$ at $a\text{H}_2\text{O} = 1$ (see above). The phase relations are presented in Fig. 1a, b.

Clinopyroxene is the liquidus phase under reducing conditions and is the second mineral after magnetite to crystallize under oxidizing conditions. The clinopyroxene saturation curves are quite similar in both experimental series, except that under reducing conditions the saturation curve is slightly shifted to lower temperatures compared to oxidized conditions. The plagioclase saturation curves are also quite similar under both redox conditions, with a marked negative slope addressing the well-known effect of H_2O on the suppression of plagioclase crystallization (e.g., Gaetani et al. 1993, Berndt et al. 2005). Similar to observations of other experimental studies in various systems (e.g., Feig et al. 2006, 2010, primitive MORB system; Almeev et al. 2012, rhyolitic system), low-Ca pyroxene has a relatively small stability field, being restricted to low melt-water content and relatively high temperature. The amount of low-Ca pyroxene crystals in the run products is very low (only one analysis per run was possible; see electronic supplementary data). The stability of quartz is directly correlated with low-Ca pyroxene stability based on the simplified peritectic reaction of enstatite to quartz (Ernst 1976). Here, in a non-ideal system with no end-member composition, a strict transition from one phase to the other does not exist and

Table 2 Experimental conditions

Sample	<i>P</i> (MPa)	<i>T</i> (°C)	Time (h) ^a	<i>c</i> H ₂ O ^b	<i>a</i> H ₂ O ^c	log <i>f</i> O ₂ ^d	Δ <i>QFM</i> ^e	Phase assemblages and proportions
<i>ΔQFM nominal = +3.2 (at aH₂O = 1)</i>								
PAR-ME-51	200	1030	72	4.5 ^h	0.86	-7.08	+3.2	Melt(98.6), Mt(1.4)
PAR-ME-52	200	1030	72	5.2	1.00	-6.96	+3.4	Melt(99.0), Mt(1.0)
PAR-ME-53	200	1030	72	2.1	0.30	-8.00	+2.3	Melt(98.1), Mt(1.9)
PAR-ME-55	200	1030	72	1.9	0.25	-8.28	+2.0	Melt(73.3), Mt(1.3), Cpx–Opx(6.4), Pl(19.0)
PAR-ME-54	200	1030	72	1.4	0.15	-8.74	+1.6	Melt(76.4), Mt(2.2), Cpx(3.9), Pl(17.5)
PAR-ME-86	100	1030	69	3.2 ^h	0.82	-6.78	+3.6	Melt(98.4), Mt(1.6)
PAR-ME-87	100	1030	69	3.7	1.00	-6.66	+3.7	Melt(98.4), Mt(1.6)
PAR-ME-88	100	1030	69	1.0	0.13	-8.41	+2.0	Melt(91.5), Mt(1.4), Cpx(1.9), Pl(5.2)
PAR-ME-90	100	1030	69	0.5	0.03	-9.60	+0.8	Melt(73.6), Mt(1.5), Cpx(4.3), Pl(20.6)
PAR-ME-89	100	1030	69	0.3	0.01	-10.58	-0.2	Melt(78.8), Mt(1.6), Cpx(7.0), Pl(12.6)
PAR-ME-92	50	1030	72	1.9	0.60	-6.47	+4.0	Melt(98.6), Mt(1.4)
PAR-ME-91	50	1030	72	1.8 ^h	0.56	-6.54	+3.9	Melt(98.1), Mt(1.9)
PAR-ME-93	50	1030	72	0.3	0.02	-9.32	+1.1	Melt(92.9), Mt(2.8), Cpx(1.0), Pl(3.3)
PAR-ME-94	50	1030	72	0.1	0.00	-11.17	-0.8	Melt(87.2), Mt(0.7), Cpx(2.9), Pl(9.3)
PAR-ME-95	50	1030	72	0.1	0.00	-12.12	-1.7	Melt(78.4), Mt(2.0), Cpx(3.1), Pl(16.5)
PAR-ME-36	200	990	115	4.4 ^h	0.84	-7.88	+3.0	Melt(98.5), Mt(1.5)
PAR-ME-37	200	990	115	4.2	0.78	-7.94	+3.0	Melt(98.4), Mt(1.6)
PAR-ME-38	200	990	115	2.3	0.34	-8.61	+2.3	Melt(79.4), Mt(3.1), Cpx(7.7), Pl(9.8)
PAR-ME-39	200	990	115	2.0	0.28	-8.79	+2.1	Melt(45.3), Mt(9.2), Cpx–Opx(4.1), Pl(41.4)
PAR-ME-40	200	990	115	1.9	0.26	-8.85	+2.1	Melt(42.4), Mt(2.3), Cpx–Opx(21.6), Pl(33.8)
PAR-ME-57 ^f	200	950 ± 20	120	5.1	1.00	-8.35	+3.2	Melt(95.2), Mt(2.4), Cpx(0.9), Ap(1.5)
PAR-ME-42 ^f	200	950	120	5.1	0.98	-8.37	+3.2	Melt(95.1), Mt(1.9), Cpx(1.2), Ap(1.8)
PAR-ME-62 ^f	200	950 ± 20	120	4.9	1.00	-8.35	+3.2	Melt(96.6), Mt(2.2), Cpx(0.5), Ap(0.7)
PAR-ME-41	200	950	120	4.8 ^h	0.92	-8.43	+3.1	Melt(93.0), Mt(2.6), Cpx(2.6), Ap(1.7)
PAR-ME-43 ^f	200	950	120	2.6	0.39	-9.38	+2.2	Melt(63.3), Mt(5.1), Cpx(6.0), Pl(25.6)
PAR-ME-44	200	950	120	2.3	0.34	-9.50	+2.0	Melt(68.1), Mt(2.7), Cpx(7.1), Pl(21.4), Qz(0.8)
PAR-ME-58 ^f	200	950 ± 20	120	2.0	0.26	-9.52	+2.0	Melt(67.7), Mt(3.8), Cpx(4.4), Pl(24.1)
PAR-ME-63 ^f	200	950 ± 20	120	1.8	0.22	-9.67	+1.9	Melt(66.6), Mt(3.1), Cpx(3.9), Pl(26.5)
PAR-ME-66 ^f	200	950 ± 20	120	0.8	0.06	-10.82	+0.7	Melt(32.0), Mt(3.7), Cpx–Opx(15.2), Pl(47.5), Qz(1.6)
PAR-ME-45 ^f	200	950	120	0.5	0.02	-11.79	-0.3	Melt(24.9), Mt(6.1), Cpx(20.9), Pl(44.1), Qz(4.0)
PAR-ME-65 ^f	200	950 ± 20	120	0.5	0.02	-11.6	-0.1	Melt(24.3), Mt(5.7), Cpx(12.9), Pl(53.0), Qz(4.2)
PAR-ME-46	200	910	144	5.3 ^h	0.99	-9.32	+2.9	Melt(90.7), Mt–Ilm(2.3), Cpx(4.1), Ap(2.9)
PAR-ME-47	200	910	144	5.1	0.95	-9.35	+2.9	Melt(90.9), Mt–Ilm(2.6), Cpx(3.8), Ap(2.7)
PAR-ME-49	200	910	144	2.2	0.31	-10.33	+1.9	Melt(55.4), Mt(3.5), Cpx(4.8), Pl(32.4), Qz(3.9)
PAR-ME-50	200	910	144	1.6	0.16	-10.88	+1.3	Melt(29.6), Mt(6.6), Cpx(21.8), Pl(35.0), Qz(7.1)
<i>ΔQFM nominal = +1 (at aH₂O = 1)</i>								
PAR-ME-27	210	1030	92	3.0	0.51	-9.27	+1.0	Melt(100)
PAR-ME-28	210	1030	92	2.7	0.44	-9.41	+0.9	Melt(100)
PAR-ME-26	210	1030	92	1.8 ^h	0.23	-9.95	+0.4	Melt(98.5), Cpx(1.5)
PAR-ME-30	210	1030	92	1.3	0.14	-10.34	±0	Melt(75.3), Cpx–Opx(4.2), Pl(20.5)
PAR-ME-29	210	1030	92	0.6	0.03	-11.59	-1.3	Melt(73.4), Cpx–Opx(6.8), Pl(19.8)
PAR-ME-11	200	990	220	5.5 ^h	1.00	-10.03	+0.9	Melt(100)
PAR-ME-12	200	990	220	5.3	1.00	-10.03	+0.9	Melt(100)
PAR-ME-13	200	990	220	2.8	0.45	-10.73	+0.2	Melt(96.2), Cpx(3.2), Pl(0.6)
PAR-ME-14	200	990	220	1.9	0.26	-11.20	-0.3	Melt(73.8), Ilm(0.6), Cpx–Opx(6.0), Pl(19.6)
PAR-ME-15	200	990	220	1.0	0.08	-12.24	-1.3	Melt(34.9), Ilm(2.8), Cpx–Opx(20.0), Pl(42.3)
PAR-ME-21	208	950	115	5.5 ^h	1.00	-10.79	+0.7	Melt(100)

Table 2 continued

Sample	<i>P</i> (MPa)	<i>T</i> (°C)	Time (h) ^a	<i>c</i> H ₂ O ^b	<i>a</i> H ₂ O ^c	log <i>f</i> O ₂ ^d	ΔQFM ^e	Phase assemblages and proportions
PAR-ME-22	208	950	115	5.2	1.00	-10.79	+0.7	Melt(100)
PAR-ME-23	208	950	115	2.1	0.28	-11.93	-0.4	Melt(77.6), Mt(1.3), Cpx–Opx(9.9), Pl(11.2)
PAR-ME-24	208	950	115	1.3	0.13	-12.62	-1.1	Melt(46.0), Mt–Ilm(1.2), Cpx–Opx(11.6), Pl(41.3)
PAR-ME-25	208	950	115	0.3	0.01	-14.89	-3.4	Melt(47.8), Ilm(1.3), Cpx–Opx(16.2), Pl(34.7)
PAR-ME-02	200	910	188	4.4	0.81	-11.06	+1.2	Melt(90.2), Mt(2.8), Cpx(4.5), Ap(2.5)
PAR-ME-01	200	910	188	4.2 ^h	0.76	-11.11	+1.1	Melt(89.4), Mt(2.8), Cpx(4.5), Ap(3.3)
PAR-ME-04	200	910	188	2.0	0.27	-12.01	+0.2	Melt(26.7), Mt(4.0), Cpx(17.8), Pl(43.5), Qz(8.1)
PAR-ME-03	200	910	188	1.6	0.17	-12.39	-0.2	Melt(28.3), Mt(2.7), Cpx–Opx(11.7), Pl(55.0), Qz(2.3)
PAR-ME-05	200	910	188	1.0	0.09	-13.01	-0.8	Melt(21.6), Mt(3.7), Cpx–Opx(17.8), Pl(51.0), Qz(5.8)
PAR-ME-71	200	850	670 ^g	5.5 ^h	1.00	-12.01	+1.3	Melt(85.4), Mt–Ilm(3.3), Cpx(5.5), Pl(4.1), Ap(1.7), Zrn
PAR-ME-72	200	850	670 ^g	5.1	0.92	-12.70	+0.6	Melt(70.6), Mt–Ilm(3.7), Cpx(5.4), Pl(17.2), Ap(3.1), Zrn
PAR-ME-81 ^f	200	800	650 ^g	5.5 ^h	1.00	-13.73	+0.6	Melt(72.5), Mt–Ilm(4.9), Cpx(8.2), Pl(14.4), Ap, Zrn
PAR-ME-101 ^f	200	800 ± 20	336 ^g	5.5 ^h	1.00	-13.77	+0.5	Melt(68.4), Mt–Ilm(5.7), Cpx(6.7), Pl(19.1), Zrn, Amp
PAR-ME-82	200	800	650 ^g	5.4	1.00	-13.73	+0.6	Melt(70.2), Mt–Ilm(3.3), Cpx(6.6), Pl(18.3), Ap(1.6), Zrn
PAR-ME-110 ^f	200	800 + 50	336 ^g	5.4	1.00	-13.77	+0.5	Melt(63.9), Mt–Ilm(3.0), Cpx(13.6), Pl(19.6)
PAR-ME-105 ^f	200	800	336 ^g	4.8 ^h	0.86	-13.89	+0.4	Melt(75.9), Mt–Ilm(3.8), Cpx(6.6), Pl(13.7), Ap, Zrn, Amp
PAR-ME-107 ^f	200	800	336 ^g	3.5	0.62	-14.19	+0.1	Melt(46.7), Mt–Ilm(5.7), Cpx(10.8), Pl(30.9), Qz(6.0)
PAR-ME-111 ^f	200	800 + 50	336 ^g	3.1	0.50	-14.37	-0.1	Melt(49.5), Mt–Ilm(6.6), Cpx(9.0), Pl(28.0), Qz(7.0), Amp
PAR-ME-103 ^f	200	800 ± 20	336 ^g	2.9	0.44	-14.48	-0.2	Melt(39.8), Mt–Ilm(6.1), Cpx(8.2), Pl(33.1), Qz(12.9), Ap, Zrn
PAR-ME-97	200	750	666 ^g	5.1	1.00	-14.95	+0.5	Melt(40.2), Ilm(7.0), Cpx(11.1), Pl(23.2), Qz(18.6), Ap, Zrn, Amp

Mt magnetite, *Ilm* ilmenite, *Cpx* clinopyroxene, *Opx* orthopyroxene, *Pl* plagioclase, *Qz* quartz, *Ap* apatite, *Zrn* zircon, *Amp* amphibole

^a Time between reaching desired temperature and rapid quench

^b Water content of the melt determined via by-difference with electron microprobe (KFT-calibrated)

^c *a*H₂O is calculated from the measured composition of the fluid phase after Burnham (1979)

^d Calculated following the procedure of Scaillet et al. (1995)

^e ΔQFM indicates log *f*O₂ (experiment) – log *f*O₂ (QFM buffer) as estimated by Schwab and Küstner (1981)

^f Data from Erdmann and Koepke (2016); if specified, temperature variations indicate temperature cycling

^g Experiments performed in CSPVs; intrinsic conditions in the CSPVs correspond to the NNO buffer (NNO ~ΔQFM+1)

^h Seawater analog (distilled water + 3.2 wt% NaCl) was added as fluid phase instead of pure water

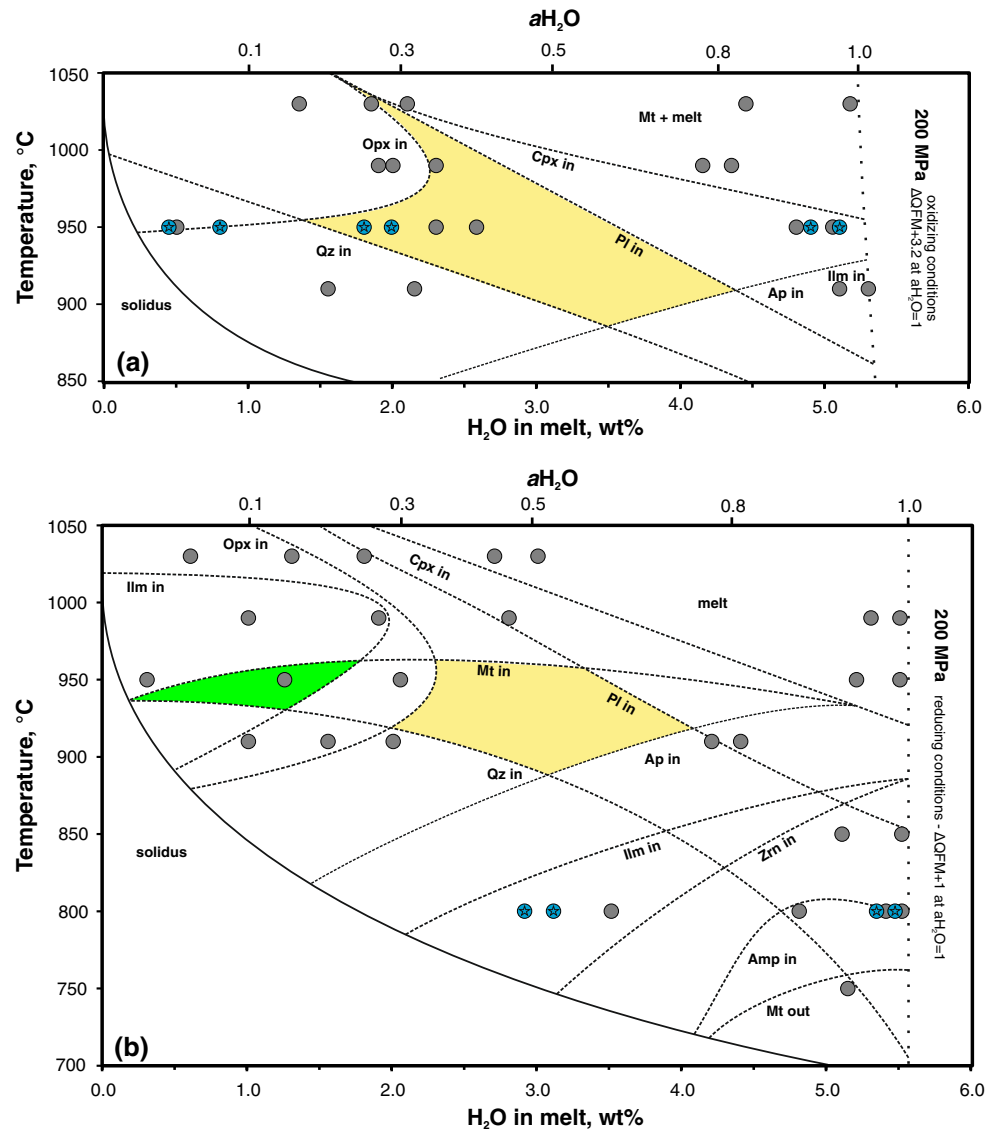
the stability fields of these two phases slightly overlap at reducing conditions. At higher *f*O₂, quartz is also stable at 950 °C. Magnetite is liquidus phase under oxidizing conditions, while under reducing conditions, magnetite crystallizes at ~950 °C and becomes unstable at *T* ≤ 750 °C. The only accessory mineral observed in the high-temperature range (i.e., 1030–910 °C in IHPVs) is apatite, in both oxidizing and reducing experiments. Zircon, as a second accessory mineral, is stable in all runs with melt H₂O > 3.5 wt%. Amphibole is the last crystallizing phase, only stable in experiments at high melt-water content (≥4.8 wt%) and low temperature (≤800 °C). The solidus is dramatically influenced by the water content, independent of redox conditions. It is shifted lower by more than 300 °C when comparing the dry system (solidus at ~1000 °C)

with water-saturated conditions (solidus at ~700 °C at melt H₂O ≈ 5.5 wt%; data only available for reducing conditions; Fig. 1b).

Phase proportions

Proportions of all phases (determined via *ImageJ*; Schneider et al. 2012; <http://imagej.nih.gov/ij/>) are listed in Table 2. The melt fraction in experiments with high *a*H₂O (>0.8) is relatively high over a large temperature range (≥64 vol% at *T* ≥ 800 °C) and decreases rapidly at *T* = 750 °C to ≤40 vol% (Fig. 2a). The melt fraction remains at a relatively high level (≥40 vol%) in experiments with a moderate water content (*a*H₂O > 0.4) at temperatures above 800 °C and also in experiments with high

Fig. 1 Phase relations determined for the PAR 3DS1 sample (dacitic composition) as a function of temperature and water content in the melt (in wt%) at **a** high initial f_{O_2} ($\Delta QFM+3.2$ at $a_{H_2O} = 1$) and **b** low initial f_{O_2} ($\Delta QFM+3.2$ at $a_{H_2O} = 1$). Each gray dot represents an experimental run (dots marked with a star are cycling experiments; see Erdmann and Koepke 2016 for details). The green field highlights conditions with the best match to phase assemblages of natural systems, the yellow field indicates the mineral assemblage observed in the natural PAR silicic lavas (see text for details). The dashed vertical line marks water saturation in each system. The experimental data and mineral abbreviations are presented in Table 2. Please note that given a_{H_2O} values are only estimated and do not exhibit a linear relationship with the melt-water content. A greatly simplified version of this phase diagram was published by Erdmann and Koepke (2016)



water contents at lower temperatures (i.e., $T = 800$ °C). However, slightly lower water contents ($a_{H_2O} < 0.4$) dramatically decrease the melt fraction down to ~20 vol% at 910 °C. This pronounced difference between experiments with high and low a_{H_2O} also accounts for the steeply sloping solidus curve (inversely proportional; $y \sim 1/x$) in the phase diagram at low water contents with differences of about 200 °C between dry conditions and 2 wt% H_2O and a moderate decrease at higher water contents (see Fig. 1).

The plagioclase fraction exhibits an inverse relationship to the trend of melt fraction, i.e., it increases with decreasing temperature. At high a_{H_2O} , low crystallization degree and higher temperature, plagioclase is not stable (Fig. 2b).

The fraction of pyroxenes is relatively low for $a_{H_2O} > 0.4$ over the complete temperature range and also shows no significant increase close to the solidus. This is

different for $a_{H_2O} < 0.4$ where the pyroxene fraction spans a large range and the increase in pyroxene fraction with decreasing temperature is much larger when compared to the wet system. The modal percentages of clinopyroxenes and orthopyroxenes are summed, as they are indistinguishable by BSE image analyses. Orthopyroxenes are, however, rare (only present as single crystals at $T \geq 910$ °C under reducing conditions, $T \geq 950$ °C at oxidizing conditions and melt $H_2O \leq 2$ wt%) and do not influence the phase proportion significantly (Fig. 2c).

The fraction of FeTi oxides remains at a relatively low level over the complete temperature range (≤ 7 vol% except for one outlier at 990 °C); also, the influence of varying a_{H_2O} is smaller than for the other phases (Fig. 2d). A significant observation is the delayed crystallization of FeTi oxides under reducing conditions and the absence of ilmenite in most experiments performed under oxidizing

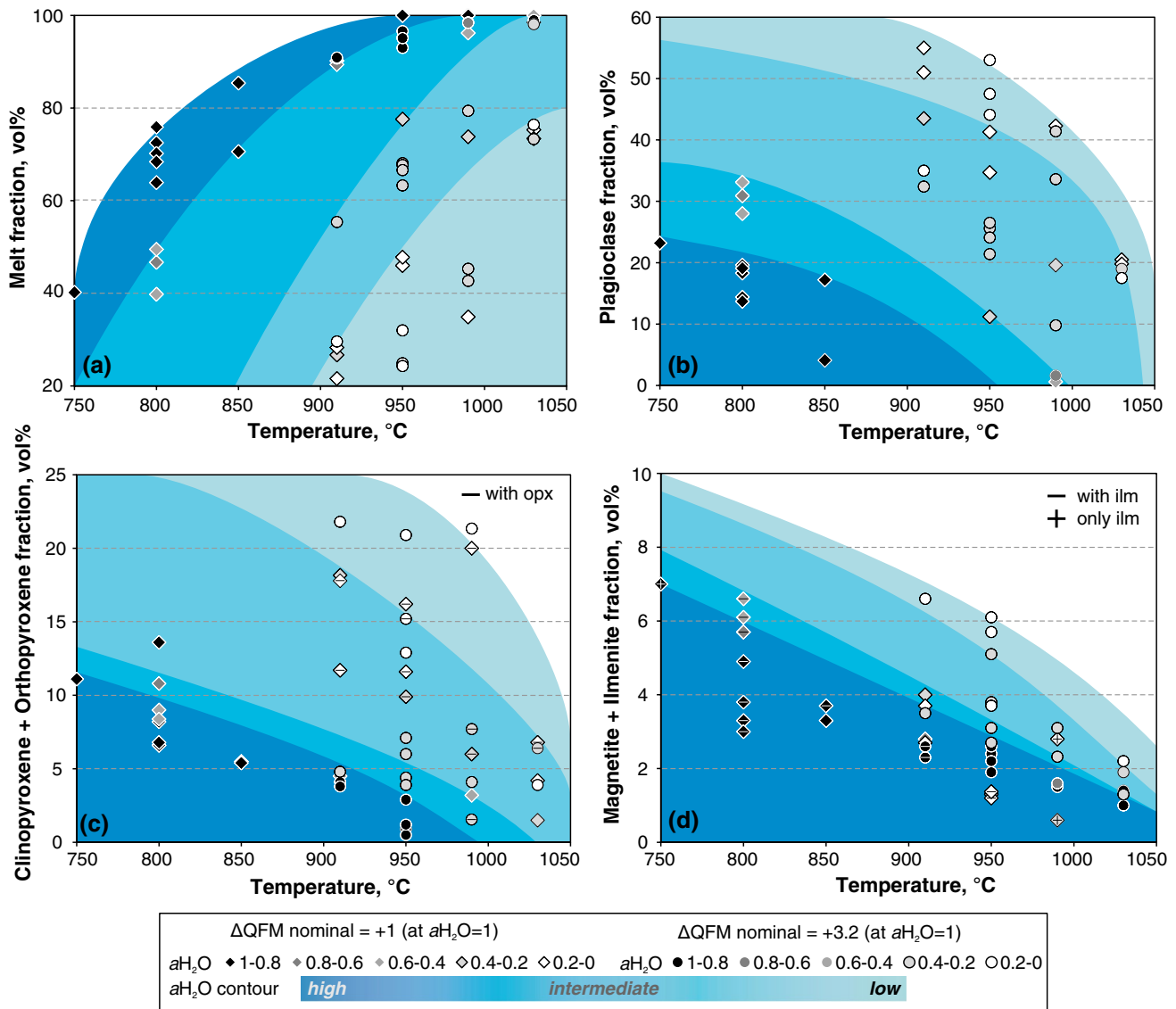


Fig. 2 Phase proportions (determined via *ImageJ*; Schneider et al. 2012; <http://imagej.nih.gov/ij/>) as a function of temperature, $f\text{O}_2$, and $a_{\text{H}_2\text{O}}$. Experiments under oxidizing conditions at 950 °C and reducing conditions at 800 °C are from Erdmann and Koepke (2016)

conditions (only present at 910 °C and high $a_{\text{H}_2\text{O}}$). However, there is no observable influence on the total FeTi oxide fraction in general if ilmenite is present.

Phase chemistry

The major element compositions of all phases with respect to temperature are given in the electronic supplementary data.

Glass

The chemical evolution of various element oxides with respect to temperature, $a_{\text{H}_2\text{O}}$, and $f\text{O}_2$ (for $T \geq 910$ °C)

is illustrated in Fig. 3. When comparing experiments performed at the same temperature, a shift to higher SiO_2 values under oxidizing conditions is visible and is most pronounced at high $a_{\text{H}_2\text{O}}$. This shift is mainly caused by the early crystallization of magnetite and, slightly delayed, clinopyroxene under oxidizing conditions, while the corresponding experiments under reducing conditions are crystal free (see also Fig. 1).

Other than the indirect effect on SiO_2 , the different applied redox conditions mainly influence the crystallization of FeTi oxides and, thus, the concentration of FeO and, to a smaller extent, TiO_2 in the melt. Most obvious is the shift of melt FeO content in less evolved, water-saturated samples. While the FeO concentration in experiments

performed under reducing conditions is close to the starting composition at higher temperature (~8 wt%) followed by a strong decrease in FeO between 950 and 910 °C with initiated FeTi oxide crystallization, the content of FeO in experiments performed under oxidizing conditions is also distinctly lower at high temperature (~6 wt%). Under reducing conditions only at low $a\text{H}_2\text{O}$, a significant increase of TiO_2 in the melt relative to the starting material is visible. This feature corresponds to a continuation of the tholeiitic trend well known from typical basaltic systems (e.g., Toplis and Carroll 1995; Berndt et al. 2005) to the more evolved system investigated here. This significant increase in TiO_2 is a consequence of the absence of FeTi oxides under these conditions and contrasts with corresponding experiments under oxidizing conditions. There, the crystallization of magnetite occurs early and incorporates up to 12.5 wt% TiO_2 , which is reflected by the decrease in melt TiO_2 content.

As expected, the Al_2O_3 concentration is enriched in those experiments in which plagioclase crystallization is delayed (i.e., at high $a\text{H}_2\text{O}$ and temperatures above 850 °C). With initiation of plagioclase crystallization at high $a\text{H}_2\text{O}$, Al_2O_3 content in the melt decreases rapidly to the same level found under H_2O -undersaturated conditions. Samples with intermediate $a\text{H}_2\text{O}$ contain less plagioclase than samples with low $a\text{H}_2\text{O}$, which is illustrated by a slower decrease in Al_2O_3 (see also phase proportions in Table 2).

The delay in plagioclase crystallization at high $a\text{H}_2\text{O}$ also affects the CaO concentrations. However, with respect to CaO in melt, clinopyroxene crystallization has a more distinct effect due to the higher concentration of CaO in clinopyroxene compared to plagioclase. Hence, CaO content in melt decreases earlier in the crystallization sequence than does Al_2O_3 content, since clinopyroxene crystallizes at a higher temperature than does plagioclase (Fig. 3). At intermediate and low $a\text{H}_2\text{O}$, clinopyroxene crystallization dominates and leads to a linear decrease in CaO. This is also valid for the decrease of melt MgO since MgO is incorporated in significant amounts exclusively in pyroxenes. K_2O is not significantly enriched in any crystalline phase; thus, the trend of K_2O reflects the degree of pure fractional crystallization (determined with the modeling program MELTS; e.g., Wanless et al. 2010), which is more pronounced at low $a\text{H}_2\text{O}$ than at lower higher water contents (Fig. 3).

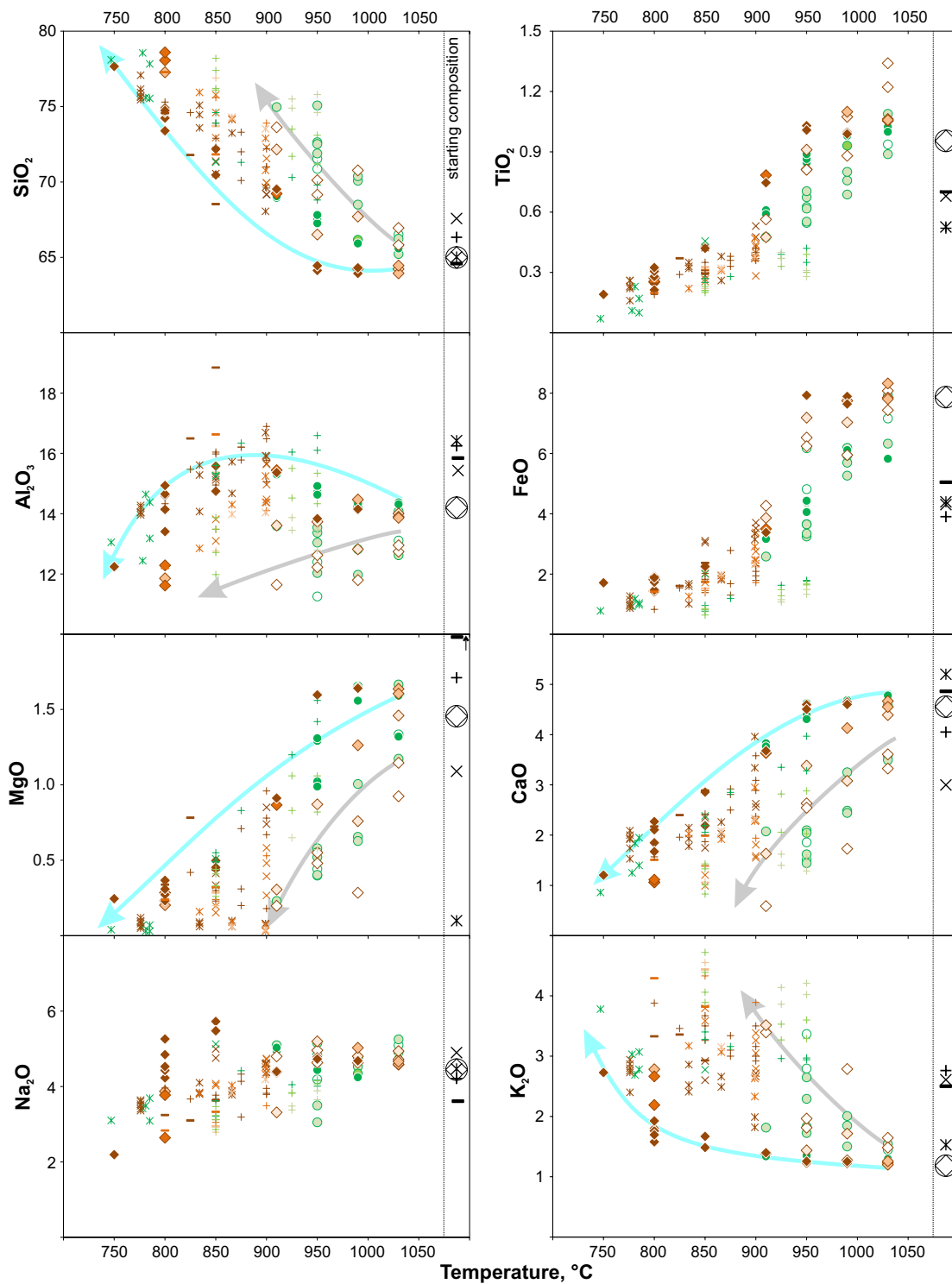
Magnetite and ilmenite

As expected from results of previous studies (e.g., Toplis and Carroll 1995; Berndt et al. 2005; Feig et al. 2010), the stability of FeTi oxides is significantly influenced by changing redox conditions. Magnetite is the dominant FeTi

oxide and is stable in all samples, at least under oxidizing conditions. Figure 4 shows the composition of the FeTi oxides, recalculated following Stormer (1983). The magnetite (MT)—ulvöspinel (USP) solid solution (X_{MT}) for all redox conditions varies from X_{MT} 0.31–0.97 (Fig. 4a). Ilmenite in the experiments performed under oxidizing conditions is rare and is characterized by a high hematite component ($X_{\text{ILM}} < 0.4$; Fig. 4b).

The MT-USP solid solution for experiments under oxidizing conditions with $a\text{H}_2\text{O} > 0.4$ is relatively high ($X_{\text{MT}} \geq 0.88$). As expected, MT crystallized at comparable $a\text{H}_2\text{O}$ but under reducing conditions shows a higher USP component with values down to $X_{\text{MT}} = 0.76$. The results show a linear trend with lower X_{MT} accompanied by lower $a\text{H}_2\text{O}$ and, thus, lower $f\text{O}_2$. Consequently, the X_{MT} in experiments with low $a\text{H}_2\text{O}$ (<0.4) and under reducing conditions varies from $X_{\text{MT}} = 0.31$ to a high of $X_{\text{MT}} = 0.61$, lower than in comparable experiments performed under oxidizing conditions ($X_{\text{MT}} = 0.86$ –0.42). However, the general trend observed under reducing conditions mirrors the trend observed under oxidizing conditions except for experiments with extremely low $a\text{H}_2\text{O}$ (Fig. 4a). Experimental MT compositions of Botcharnikov et al. (2008), who performed a phase relation study using a ferrobasalt as starting material, follow a clear linear trend toward lower X_{MT} with decreasing ΔQFM , even more pronounced than in our experimental results. However, Botcharnikov et al. (2008) did not observe any correlation in terms of $a\text{H}_2\text{O}$ and concluded that $a\text{H}_2\text{O}$ has no effect. At least for the dacitic system presented here, our results show that the influence of $a\text{H}_2\text{O}$ is obvious, irrespective of the applied initial redox condition.

With regard to the ILM-HM solid solution (Fig. 4b), experiments performed under reducing conditions and high $a\text{H}_2\text{O}$ produce ilmenites which are as hematite-rich as those produced under high $a\text{H}_2\text{O}$ and oxidizing conditions ($X_{\text{ILM}} < 0.4$). Lowering the $a\text{H}_2\text{O}$ causes an increase in the ilmenite mole fraction, up to 0.99 at $a\text{H}_2\text{O} < 0.1$. This marked step toward high X_{ILM} values proceeds exactly at the $f\text{O}_2$ of the fayalite–magnetite–quartz buffer ($\Delta\text{QFM} = 0$). Berndt et al. (2005) stated that ilmenite crystallization is less dependent on melt oxidation state but is controlled mainly by melt TiO_2 concentration, which increases with a higher degree of crystallization. Our experiments under two different redox conditions show that this conclusion has limited applicability for phase relations in a dacitic system. Since in both of our experimental series all conditions are the same except for $f\text{O}_2$, the absence of ilmenite at low melt-water content and high temperature in oxidizing experiments argues for an influence of varying redox conditions on ilmenite crystallization. This is supported by Botcharnikov et al. (2008) who showed that ilmenite is only stable in a tholeiitic system at $f\text{O}_2$



reduced conditions (ΔQFM nominal $\approx +1$ at $a_{H_2O}=1$)	oxidized conditions (ΔQFM nominal $\approx +3.2$ at $a_{H_2O}=1$)
a_{H_2O} \blacklozenge 1-0.8 $\color{orange}\lozenge$ 0.8-0.6 $\color{lightorange}\lozenge$ 0.6-0.4 $\color{yellow}\lozenge$ 0.4-0.2 $\color{lightyellow}\lozenge$ 0.2-0	a_{H_2O} \bullet 1-0.8 $\color{green}\bullet$ 0.8-0.6 $\color{lightgreen}\bullet$ 0.6-0.4 $\color{yellowgreen}\bullet$ 0.4-0.2 $\color{lightyellow}\bullet$ 0.2-0
\times Cadoux et al. (2014) — Holtz et al. (2005) + Costa et al. (2004) \times Scaillet & Evans (1999)	
<i>literature data with same coloring for redox conditions and a_{H_2O} as used for experiments of this study</i>	
\longrightarrow trend for low a_{H_2O}	\longrightarrow trend for high a_{H_2O}

Fig. 3 Compositional evolution of experimental melts as a function of temperature, fO_2 , and aH_2O . All compositions are in wt% and normalized to 100 %. For comparison, we include selected experimental results from the literature (Scaillet and Evans 1999; Costa et al. 2004; Holtz et al. 2005; Cadoux et al. 2014) using dacitic starting material at similar experimental conditions in terms of temperature, pressure, water contents and redox conditions (see text for details). Experiments under oxidizing conditions at 950 °C and reducing conditions at 800 °C are from Erdmann and Koepke (2016)

corresponding to $\Delta QFM+1$. While generally in agreement with our experiments, Botcharnikov et al. (2008) observed HM-rich oxides (low X_{ILM}) only under highly oxidized conditions ($\Delta QFM \gg 3$). Moreover, their experimental products are, in contrast to our study, independent of aH_2O ; they also detected water-saturated oxides at high ILM fractions. Here, as described already for X_{MT} , a correlation of X_{ILM} and aH_2O and, thus, redox conditions is detectable.

Seven experiments produced coexisting ilmenite and magnetite which were applied to the two-oxide geothermometer of Andersen and Lindsley (1985) using the calculation procedure of Stormer (1983). In general, the calculated temperatures are in the same range as experimental temperatures. Temperatures in experiments performed under reducing conditions are slightly overestimated by the calculation, with a larger deviation at lower temperatures ($\Delta T \approx +50$ K at 800 °C) and better consistency at higher run temperatures ($\Delta T \approx +30$ K at 850 °C and $\Delta T \approx +10$ K at 950 °C). In contrast, calculated temperatures for experiments performed under oxidizing conditions are slightly underestimated (Table 3). Redox conditions obtained from the geothermometer of Andersen and Lindsley (1985) are consistent with those experiments that are performed above 900 °C but out of the range at lower temperatures and reduced experimental conditions (Table 3).

Pyroxene

While pyroxenes in experiments with high aH_2O are exclusively clinopyroxenes (mainly augites and few diopsides), experiments performed at lower aH_2O often exhibit both clinopyroxenes and low-Ca pyroxenes (pigeonites). However, most pigeonites are relatively Ca-rich. Thus, we assume that our obtained compositions are the result of accidental detection of a pigeonite and augite combination, caused by a tiny intergrowth as previously observed by Grove and Bence (1979). Grove and Bence's (1979) experimental study interpreted pyroxenes with intermediate Ca content to be a result of microprobe analyses of overlapping clino- and orthopyroxenes. This applies to natural samples of PAR andesites, where single measurements of pyroxene are in the same range as experimental crystals. Freund et al. (2013) stated that the small (<0.2 mm) clinopyroxene minerals in the evolved lavas from the PAR are

optically and chemically zoned. The same observation was made for pyroxene analyses in andesites from the eastern Galapagos rift (Perfit and Fornari 1983) and the southern Juan de Fuca Ridge (Perfit et al. 2008).

The Mg number ($Mg\# = Mg/[Mg + Fe^{2+total}] \times 100$, molar) of all experimentally synthesized clinopyroxenes spans a wide range, from 39 to 75 (Fig. 5). Most apparent is the influence of aH_2O on Mg#. While Mg# in experiments with high aH_2O is almost constant within a wide temperature range and decreases only in the run close to the solidus (i.e., 750 °C), Mg# in experiments with lower aH_2O decreases dramatically despite little temperature variation.

Plagioclase

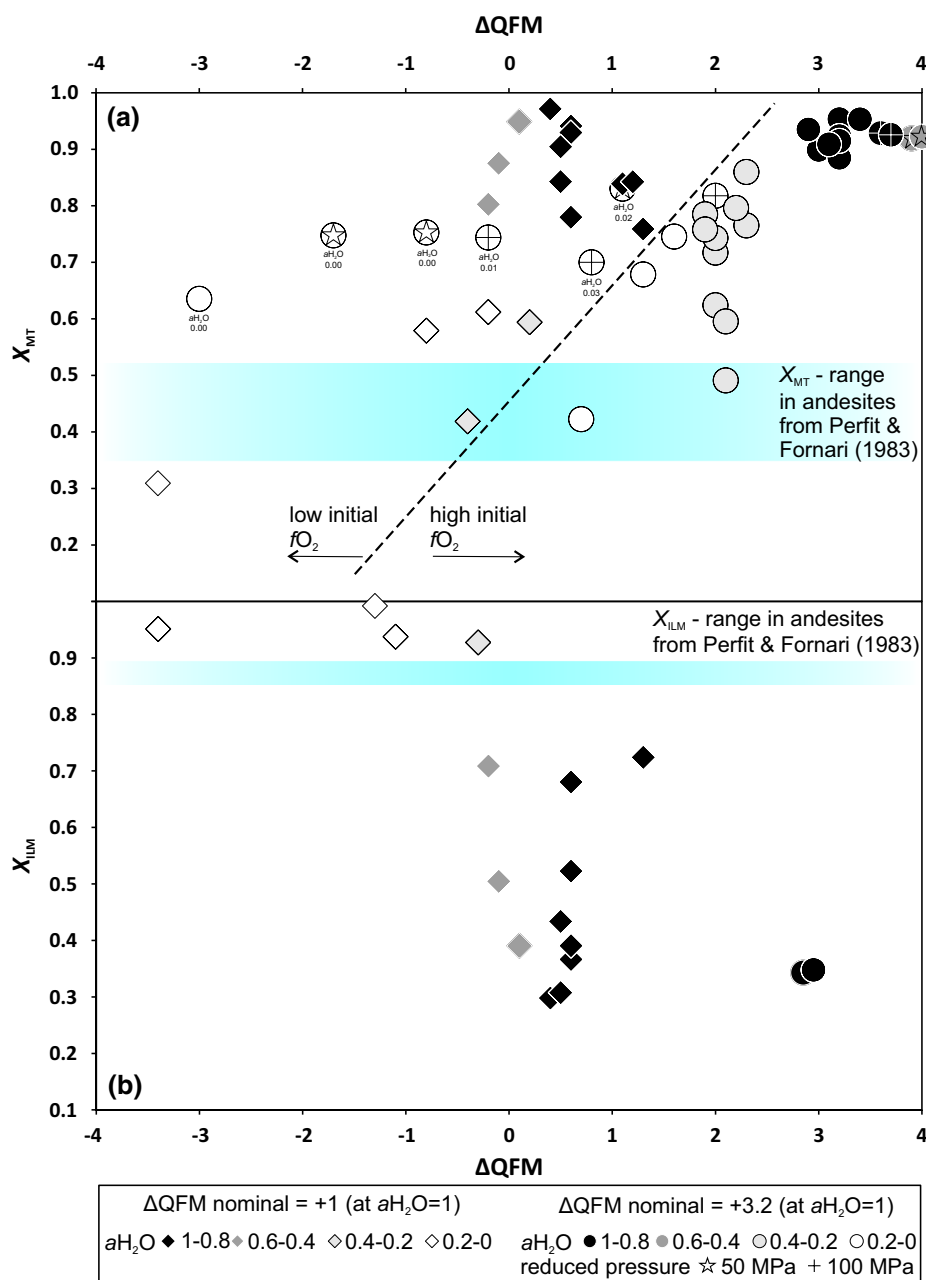
Compositions of all plagioclases relative to the Mg# of clinopyroxenes are shown in Fig. 5 as a function of melt-water activity for experiments performed under both reducing and oxidizing redox conditions. As expected, the An content decreases with decreasing temperature and decreasing aH_2O . Plagioclases from experiments with high aH_2O (i.e., >0.8) are strongly enriched in An compared to those with lower aH_2O (i.e., <0.4), which is in full agreement with previous studies (e.g., Botcharnikov et al. 2008; Feig et al. 2006; Koepke et al. 2004; Martel et al. 1998). The influence of pressure on plagioclase composition is illustrated in Fig. 5, but only for oxidizing conditions at 1030 °C and low aH_2O (i.e., <0.2), showing an apparent increase in An content with decreasing pressure. While the highest An content in a comparable experiment performed at 200 MPa is 38, the highest An content in plagioclases synthesized in experiments performed at 100 MPa is 43 and at 50 MPa is as high as 47. The An content is slightly influenced by varying fO_2 : Experiments performed under oxidizing conditions are systematically lower in An than comparable experiments (in terms of aH_2O) under reducing conditions.

Discussion

Attainment of equilibrium

Our experiments performed in IHPVs extended from 72 to 220 h (depending on temperature; cf. experimental protocol, Table 2), which is much longer than needed to reach equilibrium conditions in a basaltic system (Berndt et al. 2005; Feig et al. 2010) and is in a time frame similar to that of experiments with rhyolitic starting material conducted in the same IHPVs (Almeev et al. 2012). Experiments performed in CSPVs lasted as long as 670 h. Almeev et al. (2012) and others (e.g., Pichavant et al. 2007) showed that near-equilibrium conditions can also be reached in a

Fig. 4 Mole fractions of **a** MT in magnetite–ulvöspinel solid solution and **b** ILM in ilmenite–hematite solid solution, as a function of redox conditions (expressed as ΔQFM) and aH_2O . *Dashed line in a* separates experiments with high from those with low initial fO_2 . The *blue fields in a and b* correspond to the composition of FeTi oxides from eastern Galapagos rift andesites (Perfit and Fornari 1983). Experiments under oxidizing conditions at 950 °C and reducing conditions at 800 °C are from Erdmann and Koepke (2016)



highly evolved silicic system by using homogenized fine-grained (<200 μm) glass as starting material and choosing an appropriate run duration with regard to the expected melt viscosity.

The following observations suggest that equilibrium was obtained: (1) crystals and melt are distributed homogeneously along the capsule; (2) crystals are euhedral and chemically constant within one experimental run; (3) melt measurements are also constant within the analytical error; (4) the compositions of crystals and melt change systematically with the experimental conditions, following expected compositional trends; (5) static temperature cycling experiments were reproduced twice with the same total run

duration and consistent melt and crystal chemistry; and (6) temperatures of magnetite–ilmenite pairs calculated using different geothermometers are close to the run temperature.

Additionally, since our experiments were performed twice under oxidizing and reducing conditions, the consistency and systematics of both series' results at the same temperature suggest that equilibrium was achieved in our experiments. Even though the duration time of experiments with an H_2 control were generally longer due to slow diffusion of H_2 into the Shaw membrane, non-sensitive redox phases show identical stability curves (see below), suggesting that the chosen run times were sufficient for reaching equilibrium.

Table 3 Geothermometry of magnetite–ilmenite pairs

Sample	T (°C) exp.	T (°C) calc. ^a	$\log f_{\text{O}_2}$ ^b exp.	$\log f_{\text{O}_2}$ ^b calc. ^a
ΔQFM nominal = +3.2 (at $a_{\text{H}_2\text{O}} = 1$)				
PAR-ME-46	910	893	-9.32	-9.26
PAR-ME-47	910	880	-9.35	-9.51
ΔQFM nominal = +1 (at $a_{\text{H}_2\text{O}} = 1$)				
PAR-ME-24	950	959	-12.62	-12.30
PAR-ME-71	850	877	-12.01	-11.13
PAR-ME-72	850	878	-12.70	-10.95
PAR-ME-81 ^c	800	850	-13.73	-10.01
PAR-ME-82	800	857	-13.73	-10.03

^a Calculation of the equilibrium temperature and f_{O_2} using the geothermobarometer of Andersen and Lindsley (1985); X^{Usp} and X^{Ilm} from Stormer (1983)

^b Calculated following the procedure of Scaillet et al. (1995)

^c Experiment from Erdmann and Koepke (2016)

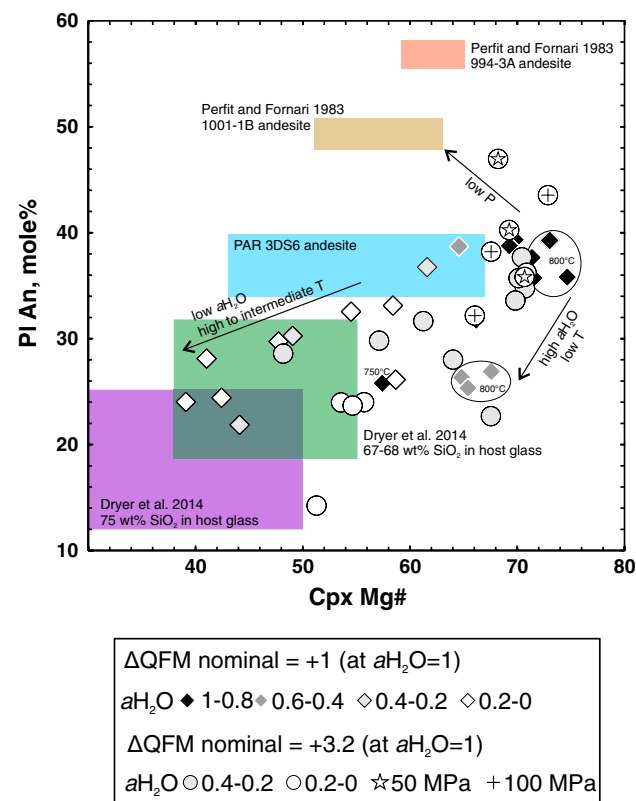


Fig. 5 An content in plagioclase versus Mg# in clinopyroxene as a function of $a_{\text{H}_2\text{O}}$ and f_{O_2} . Shown as colored fields are the phenocryst ranges of relevant natural silica-rich rocks from the oceanic crust (sample PAR 3DS6 unpublished, the others from Perfit and Fornari 1983 and Dreyer et al. 2014). Experiments under oxidizing conditions at 950 °C and reducing conditions at 800 °C are from Erdmann and Koepke (2016)

Partitioning of trace elements between melt and plagioclase

The application of the temperature cycling technique in some of our experiments resulted in increased sizes of crystals and melt pools, thus enabling the possibility of in situ trace element measurement of melt and crystals in highly evolved experiments (see Erdmann and Koepke 2016 for details). The run #110 temperature (800 °C equilibrium temperature) was periodically increased by 50 K, causing dissolution of tiny crystals in the melt and enormous growth of larger crystals, especially plagioclase. Thus, we were able to measure 19 trace elements of melt and plagioclase via SIMS in order to provide partition coefficients useful for modeling fractional crystallization processes (Table 4). The data on trace element partitioning between plagioclase ($An = 39.3$) and coexisting melt ($\text{SiO}_2 = 74.6$ wt%) of experiment #110 (see Table 2 for experimental conditions) are plotted in Fig. 6 and compared to previously published partition coefficients for plagioclase in andesitic-to-rhyodacitic melts (Severs et al. 2009 and summarized references therein). The partition coefficients determined experimentally in this study are comparable to published data with a slight tendency toward the upper limit of the range of literature values. As expected, most large ion lithophile elements (LILEs) and high field strength elements (HFSEs) behave incompatibly and are strongly enriched in the melt [Rb–Nb–Ta, Zr–Hf, heavy rare earth elements (HREEs)–Y]. Significant KD-positive anomalies relative to neighbor elements are obtained for Sr and Eu.

Comparison with other phase equilibria data in a dacitic/tonalitic system

In Fig. 3, we include data from other experimental phase relation studies (Scaillet and Evans 1999; Costa et al. 2004; Holtz et al. 2005; Cadoux et al. 2014), using dacitic starting materials that are, in terms of major elements, similar to the PAR dacite used in this study (Table 1). Starting material of these studies were obtained from different volcanos (Santorini, Unzen, San Pedro and Pinatubo) and, thus, from a different environment than the oceanic setting described in this study. Nevertheless, these studies are well eligible for comparison because applied pressures, melt-water contents, redox conditions and temperatures are at least partly in the same range as those for experiments of this study. Moreover, phase assemblages as well as phase proportions of the experimental results are similar. For a better comparability, we only used those experiments from the literature performed at $P = 200$ MPa with dry glass as starting material (all experiments are fluid-saturated).

When comparing the phase equilibria established on the Pinatubo dacite (Fig. 2 of Scaillet and Evans 1999) with

Table 4 Trace element melt composition of experiment #110 and partitioning (KD) to crystallized plagioclase

	V	Ba	Rb	Nb	Ta	La	Ce	Sr	Nd	Zr	Hf	Sm	Eu	Gd	Dy	Y	Er	Yb	Lu
Melt (ppm)	18.6	491	76.3	93.7	2.48	82.0	205	143	103	553	80.2	24.7	5.30	42.6	35.7	112	77.2	58.6	8.57
SD	2.09	0.27	2.12	0.98	0.19	0.08	0.09	0.55	0.84	7.03	4.30	0.13	0.09	4.20	0.36	0.08	1.08	2.95	0.30
KD pl-melt	0.658	0.597	0.061	0.054	0.084	0.371	0.233	7.510	0.237	0.052	0.085	0.191	0.993	0.148	0.074	0.087	0.048	0.068	0.077

the phase relations of this study (Fig. 1), two major differences are obvious: (1) slightly larger ilmenite stability field in the phase diagram of Scaillet and Evans (1999) and (2) increase in orthopyroxene stability, also at high melt H_2O contents. Both can be attributed to slightly more reduced conditions in experiments of Scaillet and Evans (1999). Costa et al. (2004) also reported a larger orthopyroxene stability field for the San Pedro dacite, even at higher fO_2 . Because experiments performed in the intermediate water content range (i.e., 2–4 wt% H_2O in the melt) at temperatures between 900 and 800 °C are lacking, it is possible that the ilmenite stability field of the PAR dacite is larger in the experimental series performed at reduced conditions. However, due to one orthopyroxene-free experiment at 900 °C and 2 wt% H_2O , the orthopyroxene stability curve was established at low melt H_2O . Other phase stability fields of both studies are in a similar range as those established for the PAR dacite.

Major element trends of most oxides presented by Scaillet and Evans (1999), Costa et al. (2004), Holtz et al. (2005) and Cadoux et al. (2014) are in general in the same range as experimental results of this study (Fig. 3). Since most experiments from the cited literature were performed at $aH_2O > 0.6$, their melt compositions mainly follow the trend for high water activities (except for Costa et al. 2004, who conducted more experiments at low $aH_2O \geq 0.4$). Pronounced discrepancies are, as expected, visible when the corresponding oxide concentration is different in the starting compositions compared to the PAR dacite of this study (e.g., MgO at Scaillet and Evans 1999, K_2O in Costa et al. 2004, Holtz et al. 2005 and Cadoux et al. 2014 and FeO in all studies used for comparison). The higher K_2O values reveal the different character of the volcanic starting materials in comparison with an oceanic environment, even though the K_2O content in the PAR dacite is already relatively high. However, most evolved samples are turning into a similar range at $T \leq 800$ °C. Even though only slightly higher in the starting compositions, literature data do not show the low Al_2O_3 range at $T \geq 900$ °C as it is produced by low aH_2O experiments of this study. While most experiments from the literature follow the trend for high aH_2O or are slightly lower (Costa et al. 2004), results of Holtz et al. (2005) show a strong enrichment despite distinct plagioclase crystallization in the corresponding phase assemblages.

Application to natural felsic lavas from mid-ocean ridges

When comparing an experimental phase equilibria study with a wide range of natural lithologies aiming to infer their pre-eruptive conditions, particular attention should be paid on the starting compositions. As demonstrated by Cadoux

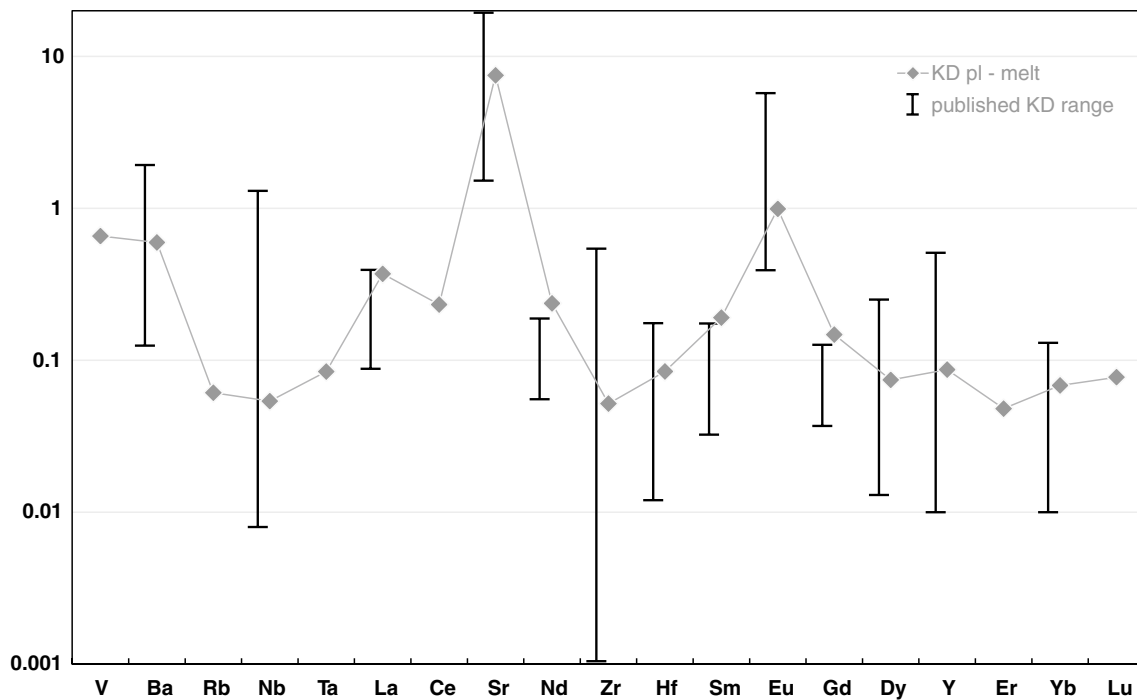


Fig. 6 Partition coefficients (KDs) for trace element partitioning between experimental melt and plagioclase of run #110 listed in Table 3 compared to published values from Severs et al. (2009) and summarized references therein. The symbols represent the average

partition coefficient determined in this study. The bold vertical line to the left of data from this study represents the complete range of partition coefficients reported in the literature

et al. (2014), small changes in whole rock compositions can affect phase relationships significantly and, hence, the inferred conditions of pre-eruptive temperature, pressure, water content and redox conditions. Cadoux et al. (2014) recommended “a case-by-case approach, whenever a precise estimate of pre-eruptive conditions is the chief objective of the experimental study.” However, our study do not primarily aims to reveal the exact pre-eruptive conditions of particular silicic magmas but rather to provide a general idea of the potential generation of felsic melts with special regard to prevailing water activities. Up to now, experimental phase relations studies in oceanic high-SiO₂ lavas have only existed for significantly higher pressures and more potassium-enriched systems. Thus, with the implication of the phase equilibria and compositions of this study, we can provide only a rough idea on formation conditions of high-silica lavas in a MOR environment based on a starting composition typically for MOR dacites (see Fig. 7), even though exact P–T–aH₂O conditions should be handled with caution.

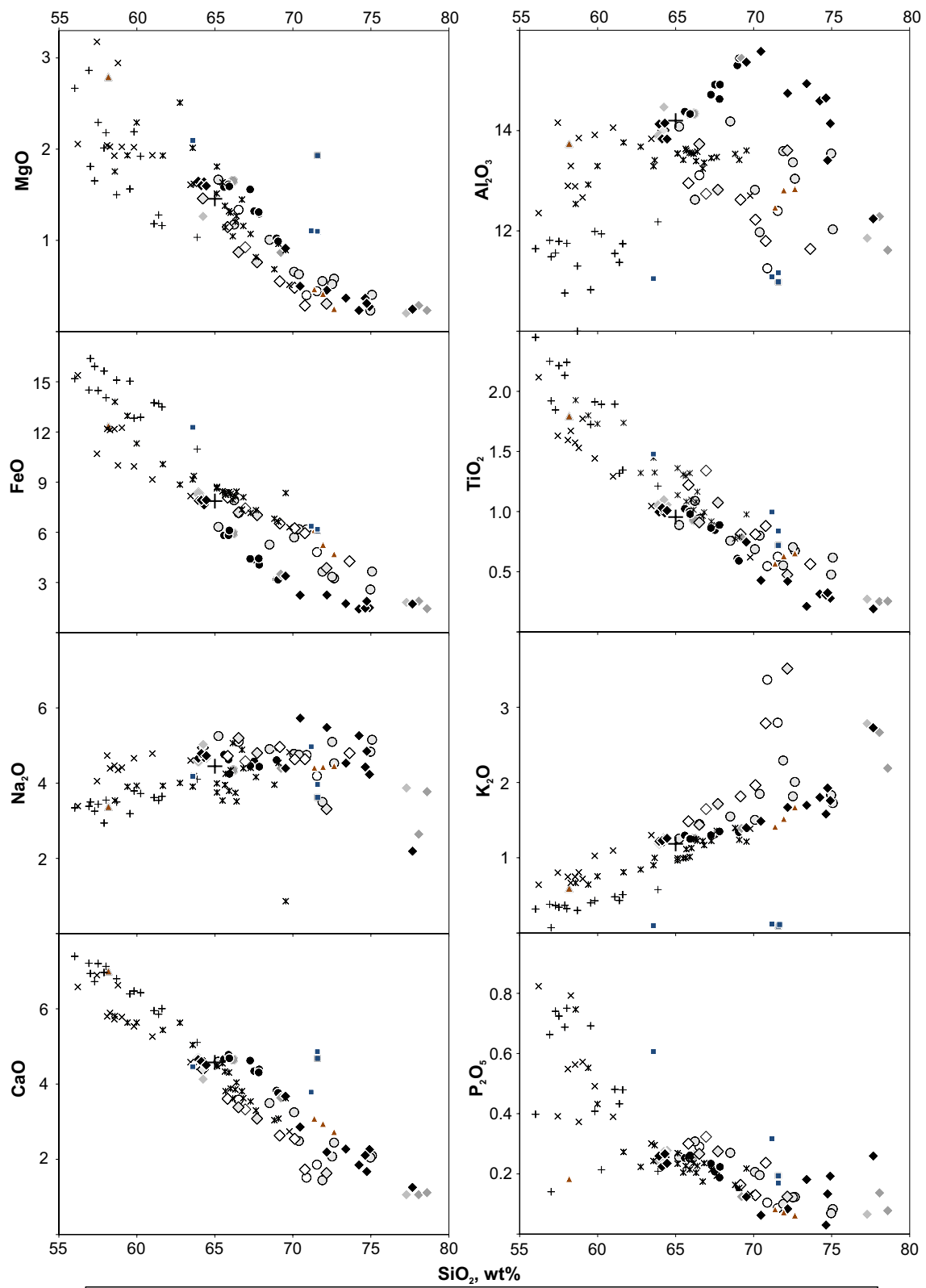
Phase equilibrium constrains on pre-eruptive conditions of PAR dacites

As described by Freund et al. (2013), the mineral assemblage in the PAR silicic lavas consists of small (~0.2 mm)

optical and chemical zoned plagioclase and clinopyroxene phenocrysts in a glassy matrix with accessory opaques (<10 μm, mainly magnetite). This mineral assemblage is reproduced in the phase equilibria at oxidized conditions as well as at reduced conditions (as indicated by the yellow fields in Fig. 1). While at oxidized conditions five experiments bear the corresponding mineral assemblage of clinopyroxene, plagioclase and magnetite, the range of the potential pre-eruptive at reduced conditions can be only indirectly inferred. Nevertheless, water contents are in both cases in the intermediate range between 2.0 and 3.5 wt% H₂O (corresponding to aH₂O of 0.3–0.6). The indicated temperature range is slightly larger at oxidized conditions (T ~1000–900 °C) than at reduced conditions (T ~950–900 °C). At these inferred conditions, the predominant mineral phase is plagioclase with ~25 vol%, followed by lower amounts of clinopyroxene (~5 vol%) and magnetite (~4 vol%, Fig. 2; Table 2). Melt proportion vary between 60 and 70 vol% which is in a comparable range to natural PAR dacites.

Phase relations of felsic lavas from MORs and inferred pre-eruptive conditions

Here, we compare our results on phase relations with other felsic lavas from actual mid-ocean ridges. For the natural



Δ QFM nominal = +1 (at $a_{H_2O}=1$) Δ QFM nominal = +3.2 (at $a_{H_2O}=1$)
 a_{H_2O} ◆ 1-0.8 ◆ 0.8-0.6 ◆ 0.6-0.4 ◇ 0.4-0.2 ◇ 0.2-0 a_{H_2O} ● 1-0.8 ● 0.8-0.6 ● 0.6-0.4 ○ 0.4-0.2 ○ 0.2-0
 + starting composition + Perfit et al. (1983, 1999) × Wanless et al. (2011)
 ▲ Byerly et al. (1976) × Freund et al. (2013) ■ Erdmann et al. (2015)

Fig. 7 Compositional evolution of experimental melts as a function of temperature, fO_2 , and aH_2O . All compositions are in wt% and normalized to 100 %. For comparison, we include data from natural silica-rich rocks from the oceanic crust published by Byerly et al. (1976), Perfit and Fornari (1983); Perfit et al. (1999), Wanless et al. (2011), Freund et al. (2013) and Erdmann et al. (2015). Experiments under oxidizing conditions at 950 °C and reducing conditions at 800 °C are from Erdmann and Koepke (2016)

evolved andesitic-to-rhyolitic system of the Alarcon Rise [northern extension of the East Pacific Rise (EPR) in the Gulf of California], a phase assemblage with dominantly plagioclase associated with titanomagnetite, ilmenite, clinopyroxene and orthopyroxene is reported (Dreyer et al. 2014). This assemblage is only reproduced under reducing conditions in a small range of temperature and melt-water content indicated by the green field in Fig. 1b. Dreyer et al. (2014) also observed fayalitic olivine, zircon and rare accessories in their studied sample suite. While zircon is stable, at least in experiments performed under high aH_2O and low temperature, olivine is absent from all our experiments.

Cotsonika et al. (2005), Perfit et al. (2008) and Werts (2012) investigated dacites from the Juan de Fuca Ridge (JdFR) and reported clinopyroxene, pigeonite, magnetite, ilmenite and plagioclase coexisting with a dacitic melt (see also Wanless et al. 2010). This phase occurrence also matches the green field in Fig. 1b, suggesting that the JdFR dacites formed under high temperatures (~950 °C) under reducing conditions at low aH_2O . The water content in basaltic andesites to dacites from the JdFR vary from 1.5 to 2.0 wt% (Werts 2012). However, the low amount of plagioclase in some JdFR dacites suggests a tendency to higher aH_2O resulting in plagioclase suppression. It is worth mentioning that also JdFR dacitic lavas bear fayalite, apatite and zircon. Fayalite and hedenbergite are not in equilibrium with the host glass leading to the assumption that the dacite is a mixing product of ferrobalt and rhyodacite (Perfit et al. 2008; Schmitt et al. 2011).

Perfit and Fornari (1983) describe Galapagos spreading center (GSC) andesites with rare phenocrysts and microphenocrysts of augite, ferroaugite, pigeonite, FeTi oxides and plagioclase. This phase assemblage also indicates formation under reducing conditions at low aH_2O , corresponding to the green field in Fig. 1b. Apatite crystals are also present in GSC andesites but are extremely rare. However, the observation of apatite by Perfit and Fornari (1983) and of zircon by Dreyer et al. (2014) accompanied by the low amount of plagioclase in some JdFR dacites reinforces the tendency to higher aH_2O . Alternatively, the crystallization of these accessories could also be a result of higher P concentration in Perfit and Fornari's (1983) system and higher Zr concentration in the system of Dreyer et al. (2014). In general, the presence of accessory minerals as apatite and

zircon should be assigned a minor role, because their stabilities are potentially strongly dependent on the composition of the protolith. For silicic lavas from the PAR, Freund et al. (2013) reported only plagioclase, clinopyroxene and accessory FeTi oxides as mineral phases, supporting crystallization conditions under higher aH_2O due to the absence of low-Ca pyroxenes.

In summary, crystallized phenocrysts and microphenocrysts in high-silica lavas from different fast- to intermediate-spreading mid-ocean ridges are experimentally reproduced only in a small range of temperature and melt-water content. The best conformity is given at a temperature of about 950 °C and melt-water contents below 2 wt%. A relatively low aH_2O is also indicated by the composition of the crystallized phases (see below). The observed accessory phases, apatite and zircon as well as the PAR phase assemblage where low-Ca pyroxene is absent (Freund et al. 2013), indicate a tendency to slightly higher aH_2O even though accessory stability should not be overstated. It should be also noted that more reducing conditions would enlarge the stability fields of ilmenite and orthopyroxene to higher water contents (e.g., Dall'Agnol et al. 1999).

Composition of the experimental phases in comparison with natural phenocrysts

The comparison to natural FeTi oxides of andesites from the eastern Galapagos rift (Perfit and Fornari 1983) reveals an agreement with our FeTi oxides generated experimentally at low aH_2O (i.e., $aH_2O < 0.4$; Fig. 4a). Because all water-rich samples show X_{MT} values >0.75 and a correlation of X_{MT} and X_{ILM} with aH_2O exists, we can conclude that a high aH_2O is an unlikely condition required for the formation of magnetite. The same conclusion can be drawn with regard to the ILM-HM solid solution, where natural ilmenites (X_{ILM} 0.86–0.90) and those from water-poor experiments (X_{ILM} 0.93–0.99) are in a similar high range, while the ILM fraction at higher aH_2O is distinctly lower (Fig. 4b).

To compare experimental plagioclases to phenocrysts observed in the glass of natural andesitic-to-rhyolitic lavas, we used the study of Perfit and Fornari (1983) as well as the study of Dreyer et al. (2014). Additionally, we show the single analysis ranges of an andesite similar to our starting material from the PAR (sample 3DS6; Fig. 5). Generally, with increasing silica content of the natural sample host glasses (Perfit and Fornari 1983, with the lowest SiO_2 content, Dreyer et al. 2014, with the highest), An content in plagioclase and Mg# in clinopyroxene decreases consistently. This linear trend is also observable in this study's experiments for crystals generated at low aH_2O (i.e., <0.4) and high to intermediate temperature (1030–910 °C). Experiments performed at lower temperature (i.e., 800 °C)

and higher melt-water content ($aH_2O > 0.4$) show Cpx Mg# that changes only slightly at a relatively high level but Pl An contents that decrease significantly. Only one water-saturated experiment close to the solidus ($T = 750$ °C) plots near the natural range of Dreyer et al. (2014). In general, their phenocrysts from the Alarcon Rise mid-ocean ridge fit our experimental crystals. This was expected, because the Dreyer et al. (2014) phenocrysts are from the most silica-rich host glasses. The high conformity with our experimental crystals generated at low aH_2O_{melt} confirms the assumption that silica-rich lavas are generated at lower aH_2O rather than under extensive hydrothermal influence.

A completely different trend can be observed for the limited number of experiments performed at lower lithostatic pressure (experiments at 50 and 100 MPa were only performed at 1030 °C). At lower pressure, the amount of water which can be incorporated into the melt is limited, and water-saturated conditions, under which plagioclase crystallization is suppressed, are rapidly reached. Thus, plagioclase only crystallizes at very low total water contents. Pressures of 100 and 50 MPa, and even lower are generally expected for the degassing history of erupted silica-rich lavas. The composition of phenocrysts in natural systems is potentially influenced by the ascent prior to eruption and does not necessarily mirror the conditions of generation deeper in the crust.

Melt compositions

In Fig. 7, we compare experimental results of this study in Harker plots for eight elements (given as their oxides) versus SiO_2 with several natural systems of evolved lavas sampled in the oceanic crust (Byerly et al. 1976; Perfit et al. 1983, 1999; Wanless et al. 2011; Freund et al. 2013; Erdmann et al. 2015). The general trend of FeO and, to a lesser extent, TiO_2 of all natural evolved lavas is congruent with those experiments performed at lower aH_2O (Fig. 7).

This observation does not hold for the K_2O trend; the compositions of natural silica-rich lavas are reproduced only by experiments performed under high aH_2O , while water-undersaturated runs exhibit higher K_2O contents. However, the K_2O content of the starting composition is relatively high at 1.2 wt%, probably caused by the influence of the Foundation hotspot chain (Haase et al. 2005; Freund et al. 2013). Thus, a strong K_2O enrichment in our experiments with low water contents is expected and does not exclude the possibility of silica-rich rock generation at low aH_2O , provided that the basaltic protolith is not enriched in K_2O due to external influence.

A clear indication of low aH_2O during the generation of evolved lavas under mid-ocean ridges is given by the Al_2O_3 content of the melts. Natural evolved systems from Byerly et al. (1976), Perfit et al. (1983, 1999), Wanless et al.

(2011), Freund et al. (2013) and Erdmann et al. (2015) all follow the trend of low aH_2O (≤ 0.4 ; Fig. 7). This indicates a relatively high amount of plagioclase in the natural rocks preventing an enrichment in Al_2O_3 as it is the case in the low aH_2O experiments of this study (see Fig. 2b). The markedly different trend at high aH_2O (> 0.4) shows that an increased Al_2O_3 with progressive crystallization (until a melt SiO_2 content of ~ 70 wt% is reached) is not reproduced by any natural system. Erdmann et al. (2015) showed a similar observation for the natural system of the EPR, where drilled tonalites (the same as those shown in Fig. 7) could be experimentally reproduced only via anatexis of a hydrothermally altered basalt at low aH_2O . Irrespective of the dominant process responsible for felsic melt generation (i.e., anatexis or fractional crystallization), it is confirmed once again that excess water is unlikely.

The differences in MgO and K_2O of the tonalites drilled from the dike/gabbro EPR transition (Erdmann et al. 2015) are eye-catching. Those samples were, in contrast to the other natural samples shown in Fig. 7, crystallized in situ within the crust and not after being erupted to the ocean floor. Thus, the influence of hydrothermal alteration is minor and the K_2O content, which can be enriched due to alteration by seawater circulation, remains low. However, Wanless et al. (2011) concluded that the high K_2O values of their natural samples from the mid-ocean ridge of the EPR are a result of partial melting and assimilation of altered oceanic crust. Here we show that K_2O values in the same range, and even higher, can be produced by extensive crystallization of an andesitic-to-dacitic rock (given that the protolith has a relatively high K_2O content; here 1.18 wt%). Despite the evolved character of the tonalites presented by Erdmann et al. (2015), the MgO content is relatively high and matches the water-saturated experiments of this study.

Chlorine enrichment due to seawater influence

The chlorine content in the natural dredged 3DS1 sample from the PAR used as starting material for this study is 1.0 wt% and after the required remelting for homogenization of the starting glass for the experiments is still 0.3 wt%. This is distinctly higher than expected for dacitic lava from fast-to-intermediate-spreading ridges containing 1.5 wt% MgO. Modeling the liquid line of descent in typical MORB with an average Cl content of 350 ppm using the MELTS program (Ghiorso and Sack 1995) leads to < 0.1 wt% Cl in fractionated melts of dacitic composition (Wanless et al. 2010). Thus, following the arguments posed by Wanless et al. (2010), silica-rich lavas with Cl contents higher than ~ 0.1 wt%, as in our 3DS1 starting material, are not believed to be generated solely by extensive fractional crystallization, but are influenced by the assimilation of hydrothermally altered wall rocks, i.e., amphibole-bearing meta-basalts or meta-gabbro

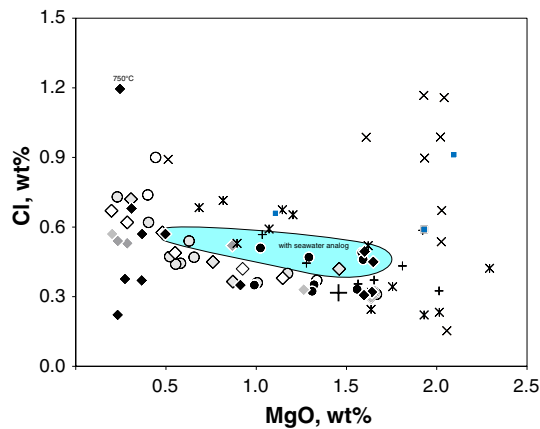


Fig. 8 Cl content (in wt%) as a function of MgO (in wt%), $a\text{H}_2\text{O}$, and $f\text{O}_2$. Data points of experiments within the *blue fields* represent those runs in which a seawater analog was added to the fluid phase (see text for details). For comparison, we include data from natural silica-rich lavas from fast- and intermediate-spreading mid-ocean ridges published by Perfit and Fornari (1983), Perfit et al. (1999), Wanless et al. (2011), Freund et al. (2013) and Erdmann et al. (2015). Experiments under oxidizing conditions at 950 °C and reducing conditions at 800 °C are from Erdmann and Koepke (2016). For legend, see Fig. 7

in the lower and mid-crust (Freund et al. 2013). Thus, here we experimentally continue the evolutionary process of fractional crystallization and simultaneously study the chemical influence of an assimilant that existed early in the evolution history on extensively evolved rocks with dacitic to rhyolitic composition. While elucidating the formation history of the starting material is beyond the aim of this study, we shed light on the Cl evolution in the experimental melts in our 3DS1 dacitic system with 0.32 wt% Cl (Fig. 8). For MgO contents higher 1.0 wt%, Cl contents of natural silica-rich lavas (Perfit and Fornari 1983; Perfit et al. 1999; Wanless et al. 2011; Freund et al. 2013; Erdmann et al. 2015) are reproduced only in those experiments in which a seawater analog was added as fluid phase instead of pure water (fluid composed of distilled water with 3.2 wt% NaCl; see “[Experimental methods](#)” section for details) in order to simulate the influence of seawater-derived hydrothermal activity. This again suggests that all known natural dacitic lavas are not formed by simple fractionation of an evolved MORB alone, but are influenced by intense Cl contamination, probably due to assimilation of hydrothermally altered material (e.g., Haase et al. 2005; Wanless et al. 2011; Freund et al. 2013). Following Kendrick et al. (2013), who studied among others basaltic glasses from the GSC, Cl contamination is not just caused by seawater contamination but rather by brine assimilation.

As melt evolution proceeds with decreasing MgO contents, the influence of added NaCl in the fluid phase on Cl enrichment in the melt becomes marginal, and the elevated Cl contents (≤ 0.9 wt%) of the most evolved natural sample

from the PAR (Freund et al. 2013) could be reproduced in experiments with low $a\text{H}_2\text{O}$ and without extra NaCl addition (Fig. 8). The melt with the highest Cl content (1.2 wt%, #97) formed in an experiment with water saturation close to the solidus without NaCl addition. This shows that during fractional crystallization hydrothermal influence is not necessarily required for enhanced Cl enrichment in a system in which Cl was already enriched in the protolith. The $a\text{H}_2\text{O}$ during the formation of silica-rich lava could be low, as demonstrated in our experiments, or it could initially be high (as in run #97), but H_2O degassed at eruption. In general, the eruptive potential is elevated due to pre-eruptive enrichments of volatiles in magmas and, thus, it controls whether the silica-rich lava erupts on the sea floor or crystallizes in situ in the deeper part of the oceanic crust. As demonstrated here, due to low $a\text{H}_2\text{O}$, CO_2 can be the dominant fluid phase. In erupted silica-rich rocks, CO_2 is mainly degassed and only moderate amounts of water are detected (1.5–2.0 wt%), but, as concluded by Wanless et al. (2011), CO_2 triggered the eruption. Hence, we propose a scenario where the water content in the fluid phase is low for evolutionary processes in the high-silica range. Hydrothermal alteration or assimilation of brine, if it occurs at all, influences primarily the basaltic protolith but plays a minor role in subsequent evolutionary processes. Thus, Cl overenrichment is possible because Cl degassing is, in contrast to H_2O degassing, insignificant (Wanless et al. 2011). The potential decoupling between these two volatiles during crustal contamination can lead to the following hypothesis: Hydrothermally altered oceanic rocks that get assimilated during magmatic evolution are Cl-rich but H_2O -poor.

The mineral assemblage of the water-rich experiment #97 also contains amphibole which has the ability to incorporate Cl. However, the Cl content of the amphibole is only 0.18 wt% (see electronic supplementary data), so the crystallization of amphibole in this experiment does not have the potential to significantly reduce the Cl content in the coexisting melt. In general, the Cl content of all analyzed amphiboles (four experiments, see electronic supplementary data) is relatively low, varying only between 0.13 and 0.19 wt%; however, the coexisting melts are strongly enriched in Cl (0.6–1.2 wt%), implying that the potential for producing amphiboles strongly enriched in Cl, as is sometimes observed in oceanic plagiogranites (e.g., Vanko 1986; Silantyev et al. 2014), is low, and other processes are more important, such as the interaction between amphibole and a high-saline fluid in the sub-solidus regime.

Conclusion

We simulated crystallization processes in a dacitic system from fast- to intermediate-spreading rate mid-ocean ridges. Results on phase relations and phase compositions can be

used to evaluate generation processes of highly evolved rocks of the oceanic crust, either erupted to the ocean floor or crystallized in situ in the mid- and lower oceanic crust. With regard to the following results, we conclude that influence by either assimilation or contamination by hydrothermally altered crust or brines is not necessarily required for felsic melt generation and relatively low $a\text{H}_2\text{O}$ can be sufficient:

- Mineral assemblages in high-silica lavas from fast- and intermediate-spreading ridges could be experimentally reproduced in a narrow range of temperature (~ 950 °C) and $a\text{H}_2\text{O}$ (<0.3) at redox conditions slightly below the QFM buffer. Even though accessory phases and the absence of low-Ca pyroxenes in some natural rocks indicate a tendency to slightly higher $a\text{H}_2\text{O}$, as proposed here water-saturated conditions are unlikely to generate the observed natural phase assemblages.
- The glass and bulk composition of felsic rocks is best reproduced in the melt of those experiments performed under low $a\text{H}_2\text{O}$ (<0.4). The strong enrichment in Al_2O_3 in high $a\text{H}_2\text{O}$ experiments, especially, contradicts natural observations.
- The strong decrease in FeO due to high water concentration as described in previous experimental studies (e.g., Feig et al. 2006; Botcharnikov et al. 2008) can be observed in the experimental melts as well. However, because natural rocks show a minor decrease in FeO, which is only reproduced in experiments at low $a\text{H}_2\text{O}$, the presence of excess water is unlikely.
- Relatively high Cl contents, as observed in natural systems ($\text{Cl} \leq 0.9$ wt%), can be reproduced in evolved melts of the crystallization experiments performed under low $a\text{H}_2\text{O}$, given early-stage Cl enrichment in the protolith, probably due to contamination of hydrothermally altered crust or brines.
- FeTi oxides, clinopyroxene and plagioclase phenocrystic compositions of natural evolved systems are only reproduced in experiments with low $a\text{H}_2\text{O}$. The presence of FeTi oxides additionally confirms the assumption that redox conditions around QFM or slightly below are most likely for the formation of silica-rich rocks because natural trends are better reproduced by experiments performed under low initial $f\text{O}_2$.

Acknowledgments We thank Otto Dietrich and Julian Feige for their careful sample preparation. We also thank the Editor J. Hoefs and the reviewers M. Perfit and B. Scaillet for their constructive comments that considerably improved the quality of this work. We gratefully acknowledge the chief scientists of RV Sonne, especially K.M. Haase, for access to the sample 3DS1 used in this study. Funding for this research was provided by grants from the Deutsche Forschungsgemeinschaft (KO 1723/13). This is CRPG Contribution Number 2461.

References

- Almeev RR, Nash BP, Holtz F, Erdmann M, Cathey HE (2012) High-temperature, low- H_2O silicic magmas of the Yellowstone hotspot: an experimental study of rhyolite from the Bruneau-Jarvis Eruptive Center, Central Snake River Plain, USA. *J Petrol* 53(9):1837–1866
- Andersen DJ, Lindsley DH (1985) New (and final!) models for the Ti-magnetite/ilmenite geothermometer and oxygen barometer. *American Geophysical Union 66* (Abstract AGU 1985 Spring Meeting Eos Transactions): 416
- Beard JS, Lofgren GE (1991) Dehydration melting and water-saturated melting of basaltic and andesitic greenstones and amphibolites at 1, 3, and 6.9 kb. *J Petrol* 32(2):365–401
- Berndt J, Liebske C, Holtz F, Freise M, Nowak M, Ziegenbein D, Hurkuck W, Koepke J (2002) A combined rapid-quench and H₂-membrane setup for internally heated pressure vessels: description and application for water solubility in basaltic melts. *Am Mineral* 87(11–12):1717–1726
- Berndt J, Koepke J, Holtz FO (2005) An experimental investigation of the influence of water and oxygen fugacity on differentiation of MORB at 200 MPa. *J Petrol* 46(1):135–167
- Botcharnikov RE, Koepke J, Holtz F, McCammon C, Wilke M (2005) The effect of water activity on the oxidation and structural state of Fe in a ferro-basaltic melt. *Geochim Cosmochim Acta* 69(21):5071–5085
- Botcharnikov RE, Almeev RR, Koepke J, Holtz F (2008) Phase relations and liquid lines of descent in hydrous ferrobasalt: implications for the Skaergaard intrusion and Columbia River flood basalts. *J Petrol* 49(9):1687–1727
- Brophy J (2008) A study of rare earth element (REE)SiO₂ variations in felsic liquids generated by basalt fractionation and amphibolite melting: a potential test for discriminating between the two different processes. *Contrib Mineral Petrol* 156:337–357
- Brophy J (2009) La–SiO₂ and Yb–SiO₂ systematics in mid-ocean ridge magmas: implications for the origin of oceanic plagiogranite. *Contrib Mineral Petrol* 158(1):99–111
- Burnham CW (1979) The importance of volatile constituents. Princeton University Press, Princeton
- Burnham CW (1994) Development of the Burnham model for prediction of H₂O solubility in magmas. In: Carroll MR, Holloway JR (eds) Volatiles in magmas. Mineralogical Society of America and Geochemical Society. *Rev Mineral Geochem* 30:123–129
- Byerly GR, Melson WG, Vogt PR (1976) Rhyodacites, andesites, ferro-basalts and ocean tholeiites from the Galapagos spreading center. *Earth Planet Sci Lett* 30(2):215–221
- Cadoux A, Scaillet B, Druitt TH, Deloué E (2014) Magma storage conditions of large Plinian eruptions of Santorini Volcano (Greece). *J Petrol* 55(6):1129–1171
- Charlier B, Namur O, Grove TL (2013) Compositional and kinetic controls on liquid immiscibility in ferrobasalt-rhyolite volcanic and plutonic series. *Geochim Cosmochim Acta* 113:79–93
- Costa F, Scaillet B, Pichavant M (2004) Petrological and experimental constraints on the pre-eruption conditions of Holocene dacite from Volcán San Pedro (36 S, Chilean Andes) and the importance of sulphur in silicic subduction-related magmas. *J Petrol* 45(4):855–881
- Cotsonika LA, Perfit MR, Smith MC, Kamenov G, Stakes D, Ridley WI, Wallace P (2005) Petrogenesis of andesites and dacites from the southern Juan de Fuca ridge. *Eos Trans. AGU* 86(52) (Fall Meet. Suppl.): Abstract V13B-0551
- Dall’Agnol R, Scaillet B, Pichavant M (1999) An experimental study of a lower proterozoic A-type granite from the Eastern Amazonian Craton, Brazil. *J Petrol* 40(11):1673–1698

- Devine JD, Gardner JE, Brack HP, Layne GD, Rutherford MJ (1995) Comparison of microanalytical methods for estimating H₂O contents of silicic volcanic glasses. *Am Mineral* 80(3–4):319–328
- Dick HJB, Natland JH, Alt JC, Bach W, Bideau D, Gee JS, Haggas S, Hertogen JGH, Hirth G, Holm PM, Ildefonse B, Iturrino GJ, John BE, Kelley DS, Kikawa E, Kingdon A, LeRoux PJ, Maeda J, Meyer PS, Miller DJ, Naslund HR, Niu Y-L, Robinson PT, Snow J, Stephen RA, Trimby PW, Worm H-U, Yoshinobu A (2000) A long in situ section of the lower ocean crust: results of ODP Leg 176 drilling at the Southwest Indian Ridge. *Earth Planet Sci Lett* 179(1):31–51
- Dixon-Spulber S, Rutherford MJ (1983) The origin of rhyolite and plagiogranite in oceanic crust: an experimental study. *J Petrol* 24(1):1–25
- Dreyer BM, Portner RA, Clague DA, Daczko N, Castillo P, Bindeman IN (2014) The complex history of Alarcón rise mid-ocean ridge rhyolite revealed through mineral chemistry. *Eos Trans. AGU (Fall Meet. Suppl.): Abstract #V31B-4746*
- Erdmann M, Koepke J (2016) Experimental temperature cycling as a powerful tool to enlarge melt pools and crystals at magma storage conditions. *Am Mineral* 101(4):960–969
- Erdmann M, Fischer L, France L, Zhang C, Godard M, Koepke J (2015) Anatexis at the roof of an oceanic magma chamber at IODP Site 1256 (equatorial Pacific): an experimental study. *Contrib Miner Petrol* 169(4):1–28
- Ernst WG (1976) *Petrologic phase equilibria*. W.H. Freeman and Co, San Francisco
- Fahey AJ, Zinner EK, Crozaz G, Kornacki AS (1987) Microdistributions of Mg isotopes and REE abundances in a Type A calcium–aluminum–rich inclusion from Efremovka. *Geochim Cosmochim Acta* 51(12):3215–3229
- Feig S, Koepke J, Snow J (2006) Effect of water on tholeiitic basalt phase equilibria: an experimental study under oxidizing conditions. *Contrib Miner Petrol* 152(5):611–638
- Feig S, Koepke J, Snow J (2010) Effect of oxygen fugacity and water on phase equilibria of a hydrous tholeiitic basalt. *Contrib Miner Petrol* 160(4):551–568
- Fornari DJ, Perfit MR, Malahoff A, Embley R (1983) Geochemical studies of abyssal lavas recovered by DSRV Alvin from eastern Galapagos rift, Inca Transform, and Ecuador Rift: 1. Major element variations in natural glasses and spacial distribution of lavas. *J Geophys Res Solid Earth* 88(B12):10519–10529
- France L, Koepke J, Ildefonse B, Cichy S, Deschamps F (2010) Hydrous partial melting in the sheeted dike complex at fast spreading ridges: experimental and natural observations. *Contrib Miner Petrol* 160(5):683–704
- France L, Koepke J, MacLeod CJ, Ildefonse B, Godard M, Deloule E (2014) Contamination of MORB by anatexis of magma chamber roof rocks: constraints from a geochemical study of experimental melts and associated residues. *Lithos* 202–203:120–137
- Freund S, Beier C, Krumm S, Haase KM (2013) Oxygen isotope evidence for the formation of andesitic–dacitic magmas from the fast-spreading Pacific–Antarctic Rise by assimilation–fractional crystallisation. *Chem Geol* 347:271–283
- Gaetani GA, Grove TL, Bryan WB (1993) The influence of water on the petrogenesis of subduction-related igneous rocks. *Nature* 365:332–334
- Gao S, Liu X, Yuan H, Hattendorf B, Günther D, Chen L, Hu S (2002) Determination of forty two major and trace elements in USGS and NIST SRM glasses by laser ablation–inductively coupled plasma–mass spectrometry. *Geostand Newslett* 26(2):181–196
- Ghiorso MS, Sack RO (1995) Chemical mass transfer in magmatic processes IV. A revised and internally consistent thermodynamic model for the interpolation and extrapolation of liquid–solid equilibria in magmatic systems at elevated temperatures and pressures. *Contrib Miner Petrol* 119(2):197–212
- Grove TL, Bence AE (1979) Crystallization kinetics in a multiply saturated basalt magma—an experimental study of Luna 24 ferrobasalt. *Lunar Planet Sci Conf* 1:439–478
- Haase KM, Stroncik NA, Hekinian R, Stoffers P (2005) Nb-depleted andesites from the Pacific–Antarctic Rise as analogs for early continental crust. *Geology* 33(12):921–924
- Hekinian R, Stoffers P, Ackermann D, Révillon S, Maia M, Bohn M (1999) Ridge-hotspot interaction: the Pacific–Antarctic Ridge and the foundation seamounts. *Mar Geol* 160(3–4):199–223
- Hellebrand E, Snow JE, Hoppe P, Hofmann AW (2002) Garnet-field melting and late-stage refertilization in ‘residual’ abyssal peridotites from the Central Indian Ridge. *J Petrol* 43(12):2305–2338
- Holtz F, Sato H, Lewis J, Behrens H, Nakada S (2005) Experimental petrology of the 1991–1995 Unzen dacite, Japan. Part I: phase relations, phase composition and pre-eruptive conditions. *J Petrol* 46(2):319–337
- Ila P, Frey FA (2000) Trace element analysis of USGS standards AGV2, BCR2, BHVO2, DTS2 and GSP2 by INAA. *J Radioanal Nucl Chem* 244(3):599–602
- Juster TC, Grove TL, Perfit MR (1989) Experimental constraints on the generation of FeTi basalts, andesites, and rhyodacites at the Galapagos Spreading Center, 85 W and 95 W. *J Geophys Res Solid Earth* 94(B7):9251–9274
- Kendrick MA, Arculus R, Burnard P, Honda M (2013) Quantifying brine assimilation by submarine magmas: examples from the Galapagos Spreading Centre and Lau Basin. *Geochim Cosmochim Acta* 123:150–165
- Koepke J, Feig S, Snow J, Freise M (2004) Petrogenesis of oceanic plagiogranites by partial melting of gabbros: an experimental study. *Contrib Miner Petrol* 146(4):414–432
- Koepke J, Berndt J, Feig S, Holtz F (2007) The formation of SiO₂-rich melts within the deep oceanic crust by hydrous partial melting of gabbros. *Contrib Miner Petrol* 153(1):67–84
- Martel C, Pichavant M, Bourdier JL, Traineau H, Holtz F, Scaillet B (1998) Magma storage conditions and control of eruption regime in silicic volcanoes: experimental evidence from Mt. Pelée. *Earth Planet Sci Lett* 156(1–2):89–99
- Perfit MR, Fornari DJ (1983) Geochemical studies of abyssal lavas recovered by DSRV Alvin from Eastern Galapagos Rift, Inca Transform, and Ecuador Rift: 2. Phase chemistry and crystallization history. *J Geophys Res Solid Earth* 88(B12):10530–10550
- Perfit MR, Fornari DJ, Malahoff A, Embley R (1983) Geochemical studies of abyssal lavas recovered from eastern Galapagos Rift, Inca transform, and Ecuador Rift: 3. Trace element abundances and petrogenesis. *J Geophys Res* 88:10–551
- Perfit MR, Ridley WI, Jonasson IR (1999) Geologic, petrologic and geochemical relationships between magmatism and massive sulfide mineralization along the eastern Galapagos Spreading Center. Volcanic-associated massive sulfide deposits. In: Barrie CT, Hannington MD (eds) *Reviews in economic geology*, vol 8, pp 75–100
- Perfit MR, Schmitt AK, Ridley WI, Rubin KH, Valley JW (2008) Petrogenesis of dacites from the southern Juan de Fuca Ridge. *Goldschmidt Conference Abstracts*, p 22
- Pichavant M, Costa F, Burgisser A, Scaillet B, Martel C, Poussineau S (2007) Equilibration scales in silicic to intermediate magmas—implications for experimental studies. *J Petrol* 48(10):1955–1972
- Pitzer KS, Sterner SM (1995) Equations of state valid continuously from zero to extreme pressures with H₂O and CO₂ as examples. *Int J Thermophys* 16(2):511–518
- Raczek I, Jochum KP, Hofmann AW (2003) Neodymium and strontium isotope data for USGS reference materials BCR-1, BCR-2, BHVO-1, BHVO-2, AGV-1, AGV-2, GSP-1, GSP-2 and eight MPI-DING reference glasses. *Geostand Newslett* 27(2):173–179

- Scailliet B, Evans BW (1999) The 15 June 1991 eruption of Mount Pinatubo. I. Phase equilibria and pre-eruption P–T–fO₂–fH₂O conditions of the dacite magma. *J Petrol* 40(3):381–411
- Scailliet B, Pichavant M, Roux J (1995) Experimental crystallization of leucogranite magmas. *J Petrol* 36(3):663–705
- Schmitt AK, Perfit MR, Rubin KH, Stockli DF, Smith MC, Cotsonika LA, Zellmer GF, Ridley WI, Lovera OM (2011) Rapid cooling rates at an active mid-ocean ridge from zircon thermochronology. *Earth Planet Sci Lett* 302(3):349–358
- Schneider CA, Rasband WS, Eliceiri KW (2012) NIH Image to ImageJ: 25 years of image analysis. *Nat Methods* 9(7):671–675
- Schwab RG, Küstner D (1981) Die Gleichgewichtsfugazitäten technologisch und petrologisch wichtiger Sauerstoffpuffer. *Neues Jahrb Mineral Abh* 140:111–142
- Severs MJ, Beard JS, Fedele L, Hanchar JM, Mutchler SR, Bodnar RJ (2009) Partitioning behavior of trace elements between dacitic melt and plagioclase, orthopyroxene, and clinopyroxene based on laser ablation ICPMS analysis of silicate melt inclusions. *Geochim Cosmochim Acta* 73(7):2123–2141
- Shaw HR, Wones DR (1964) Fugacity coefficients for hydrogen gas between 0 degrees and 1000 degrees C, for pressures to 3000 atm. *Am J Sci* 262(7):918–929
- Silantyev SA, Koepke J, Ariskin AA, Anosova MO, Krasnova EA, Dubinina EO, Suhr G (2014) Geochemical nature and age of the plagiogranite-gabbro association of the oceanic core complex of the Mid-Atlantic ridge at 5°10'S. *Petrology* 22(2):109–127
- Sinton JM, Detrick RS (1992) Mid-ocean ridge magma chambers. *J Geophys Res* 97(B1):197–216
- Sisson TW, Grove TL (1993) Experimental investigations of the role of H₂O in calc-alkaline differentiation and subduction zone magmatism. *Contrib Miner Petrol* 113(2):143–166
- Stakes DS, Perfit MR, Tivey MA, Caress DW, Ramirez TM, Maher N (2006) The cleft revealed: geologic, magnetic, and morphologic evidence for construction of upper oceanic crust along the southern Juan de Fuca Ridge. *Geochem Geophys Geosyst*. doi:10.1029/2005GC001038
- Stormer JC Jr (1983) The effects of recalculation on estimates of temperature and oxygen fugacity from analyses of multicomponent iron-titanium oxides. *Am Mineral* 68:586–594
- Strnad L, Mihaljevic M, Sebek O (2005) Laser ablation and solution ICP-MS determination of rare earth elements in USGS BIR-1G, BHVO-2G and BCR-2G glass reference materials. *Geostand Geoanal Res* 29(3):303–314
- Toplis MJ, Carroll MR (1995) An experimental study of the influence of oxygen fugacity on Fe–Ti oxide stability, phase relations, and mineral/melt equilibria in ferro-basaltic systems. *J Petrol* 36(5):1137–1170
- Toplis MJ, Carroll MR (1996) Differentiation of ferro-basaltic magmas under conditions open and closed to oxygen: implications for the Skaergaard intrusion and other natural systems. *J Petrol* 37(4):837–858
- Vanko DA (1986) High-chlorine amphiboles from oceanic rocks: product of highly-saline hydrothermal fluids? *Am Mineral* 71(1–2):51–59
- Veksler IV, Dorfman AM, Borisov AA, Wirth R, Dingwell DB (2007) Liquid immiscibility and the evolution of basaltic magma. *J Petrol* 48(11):2187–2210
- Wanless VD, Perfit MR, Ridley WI, Klein E (2010) Dacite petrogenesis on mid-ocean ridges: evidence for oceanic crustal melting and assimilation. *J Petrol* 51(12):2377–2410
- Wanless VD, Perfit MR, Ridley WI, Wallace PJ, Grimes CB, Klein EM (2011) Volatile abundances and oxygen isotopes in basaltic to dacitic lavas on mid-ocean ridges: the role of assimilation at spreading centers. *Chem Geol* 287(1–2):54–65
- Werts KR (2012) Phase chemistry and petrogenesis of dacitic lavas from the southern Juan de Fuca Ridge. A thesis presented to the graduate school of the University of Florida in partial fulfillment of the requirements for the degree of Master of Science, 86 pp
- Wilson SA (1997) Data compilation for USGS reference material BHVO-2, Hawaiian basalt. US geological survey open-file report 2-3
- Wilson DS, Teagle DAH, Alt JC, Banerjee NR, Umino S, Miyashita S, Acton GD, Anma R, Barr SR, Belghoul A, Carlot J, Christie DM, Coggon RM, Cooper KM, Cordier C, Crispini L, Durand SR, Einaudi F, Galli L, Gao Y, Geldmacher J, Gilbert LA, Hayman NW, Herrero-Bervera E, Hirano N, Holter S, Ingle S, Jiang S, Kalberkamp U, Kerneklia M, Koepke J, Laverne C, Vasquez HLL, MacLennan J, Morgan S, Neo N, Nichols HJ, Park S-H, Reichow MK, Sakuyama T, Sano T, Sandwell R, Scheibner B, Smith-Duque CE, Swift SA, Tartarotti P, Tikku AA, Tominaga M, Veloso EA, Yamasaki T, Yamazaki S, Ziegler C (2006) Drilling to gabbro in intact ocean crust. *Science* 312(5776):1016–1020